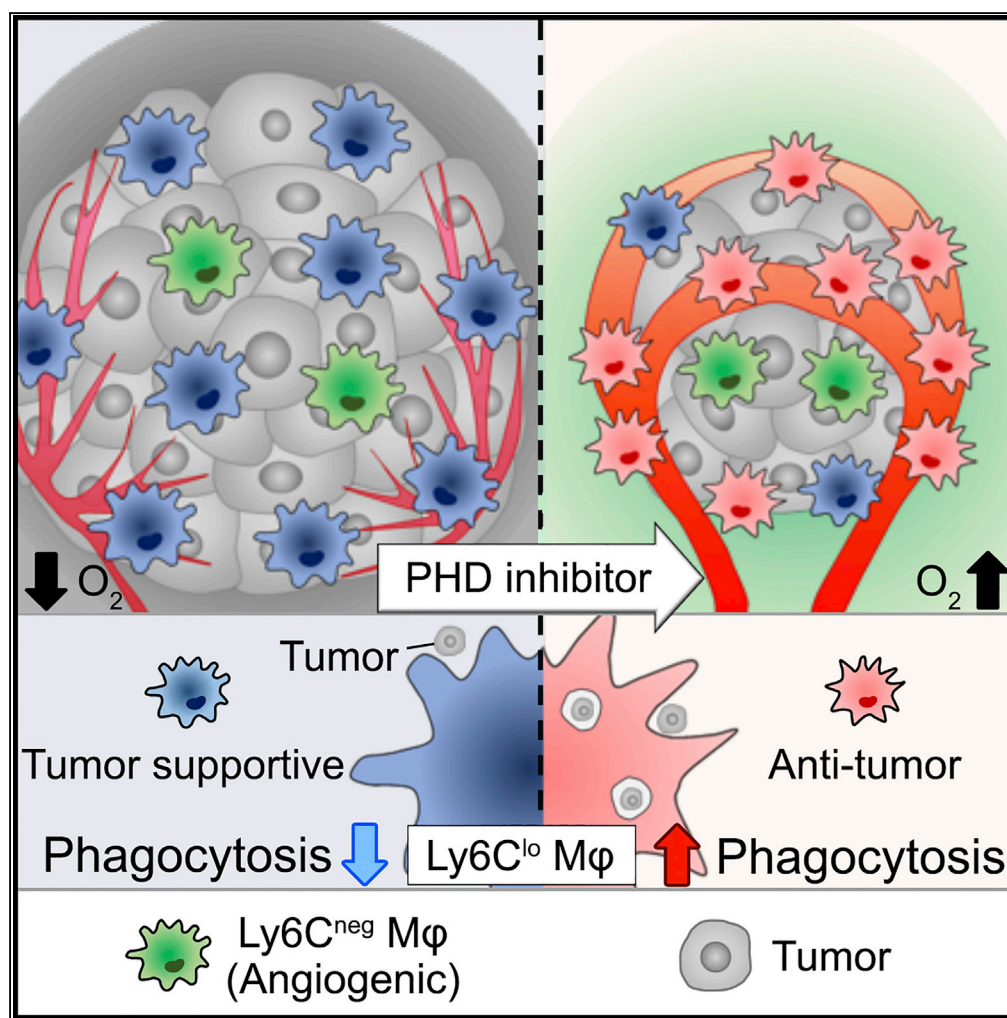**Article**

Controlling the Phenotype of Tumor-Infiltrating Macrophages via the PHD-HIF Axis Inhibits Tumor Growth in a Mouse Model

Shunji Nishide,
Shinji Matsunaga,
Masayuki
Shiota, ...,
Katsuyuki Miura,
Tatsuya Nakatani,
Shuhei Tomita

tomita.shuhei@med.osaka-cu.ac.jp

HIGHLIGHTS

PHD inhibitor treatment inhibits tumor growth and prolongs survival time of mice

Regulating the PHD-HIF pathway can alter the tumor-infiltrating macrophage phenotype

PHD inhibitor activates the tumor phagocytic ability of Ly6C^{lo} macrophages

Article

Controlling the Phenotype of Tumor-Infiltrating Macrophages via the PHD-HIF Axis Inhibits Tumor Growth in a Mouse Model

Shunji Nishide,[1,2,9] Shinji Matsunaga,[1,9] Masayuki Shiota,[3] Takehiro Yamaguchi,[1] Shojiro Kitajima,[1] Yoichi Maekawa,[4,5] Norihiko Takeda,[6] Michio Tomura,[7] Junji Uchida,[2] Katsuyuki Miura,[8] Tatsuya Nakatani,[2] and Shuhei Tomita[1,10,*]

SUMMARY

The tumor microenvironment (TME) polarizes tumor-infiltrating macrophages toward tumor support. Macrophage-abundant tumors are highly malignant and are the cause of poor prognosis and therapeutic resistance. In this study, we show that the prolyl hydroxylase (PHD) inhibitor FG-4592 (FG) inhibits tumor growth of macrophage-abundant tumors and prolongs mouse survival. FG not only normalizes tumor vessels and improves tumor oxygenation but also directly affects macrophages and activates phagocytosis through the PHD-hypoxia-inducible factor (HIF) axis. Remarkably, FG can promote phagocytic ability of the Ly6C^{lo} subset of tumor-infiltrating macrophages, leading to tumor growth inhibition. Moreover, Ly6C^{neg} macrophages contributed to blood vessel normalization. Using a malignant tumor mouse model, we characterized macrophage function and subsets. Altogether, our findings suggest that the PHD inhibitor can promote the anti-tumor potential of macrophages to improve cancer therapy.

INTRODUCTION

Tumor vessel structure differs from normal vessel structure in terms of short lumen diameter, irregular sprouting, and poor tight junction formation. This leads to leaky tumor vessels with low blood flow (Jain, 2014). These tumor microenvironments (TMEs) lead to hypoxia and high interstitial pressure, wherein immune cells exhibit impaired cytotoxicity and pathogen recognition systems. Therefore, repair of blood vessel function and normalization of the microenvironment in tumors are expected to enhance anti-tumor immunity (Quail and Joyce, 2013; Tian et al., 2017; Park et al., 2016).

Macrophages (Mφs) are the most abundant immune cells in tumors (Movahedi et al., 2010). Moreover, tumor Mφs, referred to as tumor-associated macrophages (TAMs), have been canonically classified into the inflammatory (M1) or anti-inflammatory (M2) phenotype. M1 Mφs are characterized as having high phagocytic ability and inhibitory activity toward tumor growth (Guerriero et al., 2017). In contrast, M2 Mφs, which are strongly polarized by the TME, promote tumor progression and metastasis (Henze and Mazzone, 2016; Mosser and Edwards, 2008). In addition, M2 Mφs exclude cytotoxic lymphocytes from tumors such as lung carcinomas, melanomas, and colorectal carcinomas, which are classified as TAM-abundant tumors exhibiting a low number of T cells. These phenomena are associated with tumor malignancy and result in therapeutic resistance (Binnewies et al., 2018). Therefore, there is a need for new therapeutic strategies against these tumors.

Hypoxia inducible factors (HIFs) are master regulators of the cellular response to hypoxia (Imtiyaz and Simon, 2010). HIF stability is post-transcriptionally regulated by oxygen availability through prolyl hydroxylase (PHD). If the oxygen concentration is reduced, PHDs become inactive, resulting in HIF accumulation (Semenza, 2012). HIF-1 is widely expressed and is detected in virtually all innate and adaptive immune populations including Mφs. For Mφs, the function of HIF-1 is to increase aggregation, invasion, and motility and drive the expression of proinflammatory cytokines (Nizet and Johnson, 2009; Palazon et al., 2014). Conversely, for cancer cells, HIFs control the expression of crucial genes involved in proliferation and metastasis of cancer cells (Keith et al., 2011). Therefore, the effect of simultaneously raising HIF levels in both immune cells and cancer cells on tumors remains unclear. Moreover, some reports have argued that normalization of tumor vessels results in accelerated tumor progression (Du et al., 2008; Stockmann

[1]Department of Pharmacology, Osaka City University Graduate School of Medicine, Osaka 545-8585, Japan

[2]Department of Urology, Osaka City University Graduate School of Medicine, Osaka 545-8585, Japan

[3]Division of Research Support Platform, Osaka City University Graduate School of Medicine, Osaka 545-8585, Japan

[4]Department of Parasitology and Infectious Diseases, Gifu University Graduate School of Medicine, Gifu 501-1194, Japan

[5]Domain of Integrated Life Systems, Center for Highly Advanced Integration of Nano and Life Sciences, Gifu University, Gifu 501-1193, Japan

[6]Department of Cardiovascular Medicine, Graduate School of Medicine, The University of Tokyo, Tokyo 113-8655, Japan

[7]Laboratory of Immunology, Faculty of Pharmacy, Osaka Ohtani University, Osaka 584-8540, Japan

[8]Department of Applied Pharmacology and Therapeutics, Osaka City University Graduate School of Medicine, Osaka 545-8585, Japan

[9]These authors contributed equally

[10]Lead Contact

*Correspondence: tomita.shuhei@med.osaka-cu.ac.jp

https://doi.org/10.1016/j.isci.2019.08.033

et al., 2008). Therefore, it is also unclear whether vessel normalization is beneficial for tumor progression. In this study, we examined the effect of the PHD inhibitor on tumor growth by administering FG-4592 (FG), which is currently under investigation in a phase 3 clinical trial for the treatment of anemia in chronic kidney disease (Besarab et al., 2016; Provenzano et al., 2016).

RESULTS

FG Treatment Inhibits Tumor Growth in Lewis Lung Carcinoma and B16F10 Tumors

To examine the effects of the PHD inhibitor on tumors, we used a syngeneic murine tumor model of the Lewis lung carcinoma (LLC) cell line. FG-treated mice showed significantly inhibited tumor growth (Figures 1A–1C) that was dose-dependent (Figures S1A and S1B). To examine whether this tumor growth inhibition was also exhibited in other tumor models, B16F10 melanoma and MC38 colon tumor models were used. B16F10 tumor growth was significantly inhibited by FG treatment (Figures 1D–1F), but there were no significant differences in inhibition in the MC38 tumor model (Figures S1C and S1D). Furthermore, repeated FG treatment inhibited tumor growth and prolonged survival; however, the tumor regrew on day 22 after a single FG treatment (Figures 1G and 1H). To determine whether FG induced apoptosis or inhibited proliferation of tumor cells, tumor tissues were stained with anti-cleaved caspase 3 and anti-Ki-67 antibodies (Figures 1I–1L and S1E–S1H) and a cell proliferation assay was performed *in vitro* (Figure S1I); these experiments revealed no significant differences after FG treatment. Therefore, FG treatment-induced tumor growth inhibition was not due to apoptosis or inhibited proliferation in tumor cells. We also analyzed cytokine concentrations in blood plasma and found that the cytokine signatures remained largely unaffected by FG treatment (Figure S1J). Taken together, these results suggest that FG may not directly affect tumor cells and plasma cytokines.

FG Treatment Improves TME

To investigate the indirect ways in which FG might inhibit tumor growth, we tested whether FG affected tumor vessels and the TME; TME normalization is known to have an anti-tumor effect and can reeducate immune cells (Quail and Joyce, 2013). Remarkably, we found that FG treatment drastically altered vessel structures, as tumor vessel density was significantly decreased, whereas the vessel luminal area was increased (Figures 2A and 2B). We then examined the reversibility of this alteration and found that tumor vessel structure of one-time FG-treated tumors reverted to that of vehicle control tumor vessels on day 19 (Figures S2A and S2B); however, tumors treated with FG repeatedly sustained normal vessel structure even by day 23 (Figures S2C and S2D). To assess vessel maturation, we examined tight junction formation and pericyte coverage rate with ZO-1 and NG2, respectively, whose levels were significantly increased after FG treatment (Figures 2C–2F). We also evaluated the effect of FG treatment on vessel structure in other tumor models and found that the B16F10 tumor model also exhibited changes to vessel structure following treatment (Figures S2E and S2F). Even the MC38 tumor model, in which no significant difference in tumor growth inhibition was observed after FG treatment, showed changes in vessel structure (Figures S2G and S2H). To assess whether the reconstituted tumor vessel had normal function, we evaluated tumor vessel function with high-molecular-weight dextran. Tumor tissue perfusion was recovered after FG treatment (Figure 2G, low-power field). Dextran leakage was observed in the vehicle controls as a hazy green area; in contrast, FG-treated tumor vessels showed recovered vessel function (Figure 2G, high-power field). Furthermore, hypoxic regions were significantly reduced in FG-treated mice (Figures 2H and 2I). Taken together, these results suggest that FG treatment induces TME improvement through tumor vessel normalization.

FG Treatment Induces Mφ Infiltration in Tumors and Inhibits Tumor Growth through Mφs

Next, we examined whether TME improvement by FG leads to changes in the immune cell response. We found that FG-treated tumors showed an increased CD45^{+} leukocyte cell population ratio (Figure 3A) with a significantly increased CD45^{+} CD11b^{+} F4/80^{+} Mφ cell population ratio (Figure 3B); in contrast, the T cell population did not show significant changes and had a low population of tumor-infiltrating T cells (Figure 3C). Furthermore, T cells displayed no significantly activated profiles as measured by CD69 and CD25 expression (Figure S3J). An increased number of Mφs was also observed in the tumor tissue by immunofluorescence staining (Figures 3D and 3E). These findings indicate that the LLC tumor was TAM abundant and contained few activated T cells. To determine whether FG treatment promoted proliferation of tumor-infiltrating Mφs, tumor tissues were stained with anti-F4/80 anti-Ki-67 antibodies. There were no significant differences in Mφ proliferation in tumor tissue after FG treatment (Figures S3C and S3D). Furthermore, we
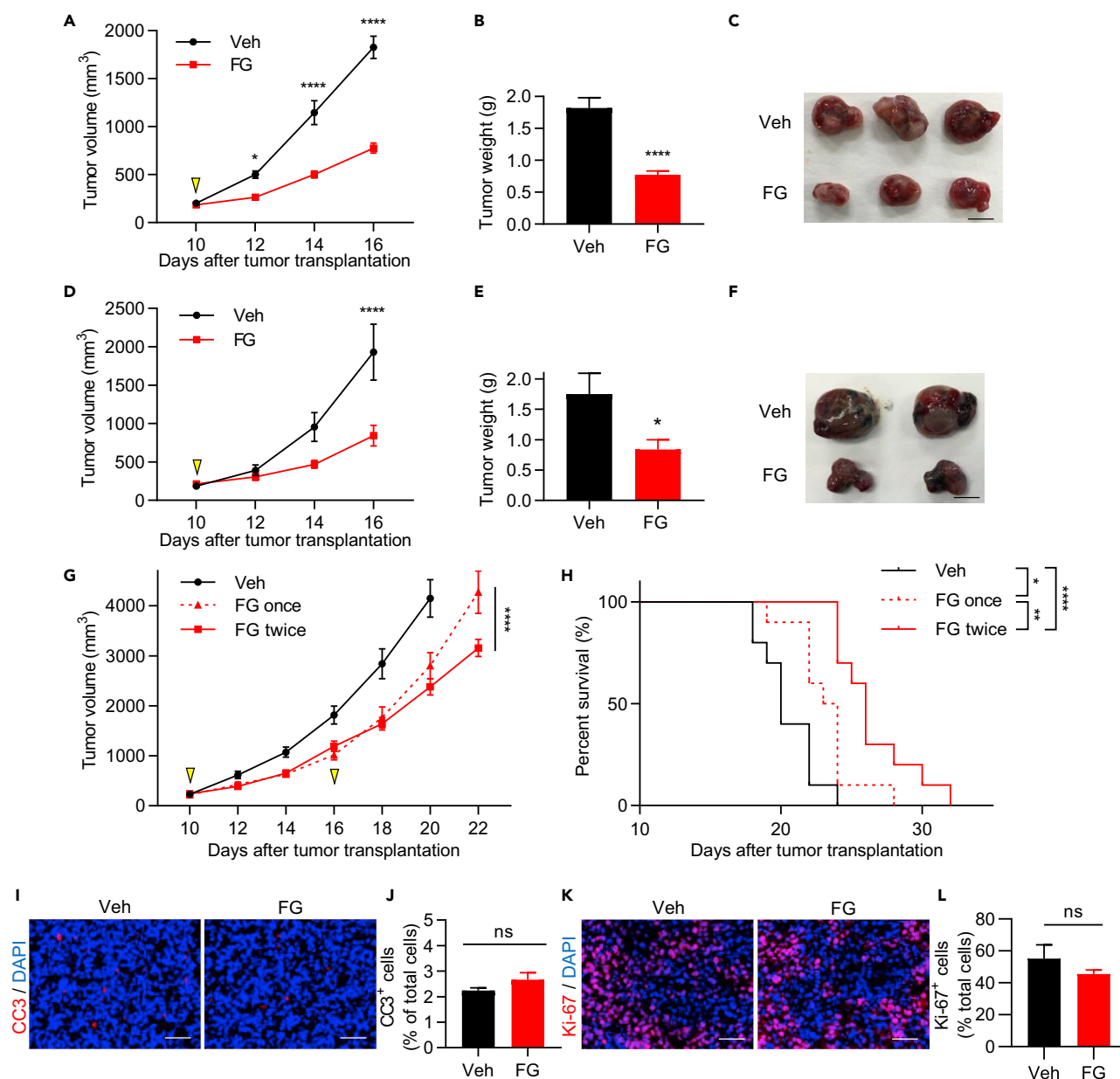
Figure 1. FG Treatment Inhibits Tumor Growth in LLC and B16F10 Tumors

(A) LLC tumor growth curves. Treatment with vehicle (Veh) or FG (3 mg; treated on day 10; n = 15).

(B) LLC tumor weight on day 16 (n = 15).

(C) Images of LLC tumors on day 16. Scale bar, 1 cm.

(D) B16F10 tumor growth curves. Treatment with Veh or FG (3 mg; treated on day 10); n = 8.

(E) B16F10 tumor weight on day 16 (n = 8).

(F) Images of B16F10 tumors on day 16. Scale bar, 1 cm.

(G) LLC tumor growth curves. Treatment with Veh (n = 11), FG (3 mg; treated once on day 10; n = 9), or FG twice (3 mg; treated on day 10 and 16; n = 11).

(H) Kaplan-Meier curves showing events-free survival rate of vehicle-, 3 mg FG once-, or 3 mg FG twice-treated mice (n = 10).

(I) Immunofluorescence (IF) images of cleaved caspase-3 (CC3; red)-stained sections of LLC tumors on day 12. Scale bar, 50 μm.

(J) Quantification of the CC3$^+$ cell ratio of total cells on day 12 (n = 3).

(K) IF images of Ki-67 (red)-stained sections of LLC tumors on day 12. Scale bar, 50 μm.

(L) Quantification of the Ki-67$^+$ cell ratio of total cells on day 12 (n = 3).

Data represent means ±SEM; two-way ANOVA (A, D, and G); Mann-Whitney test (B, E, J, and L); Log rank test (H). ns, not significant; *p < 0.05; **p < 0.01; ****p < 0.0001. See also Figure S1.
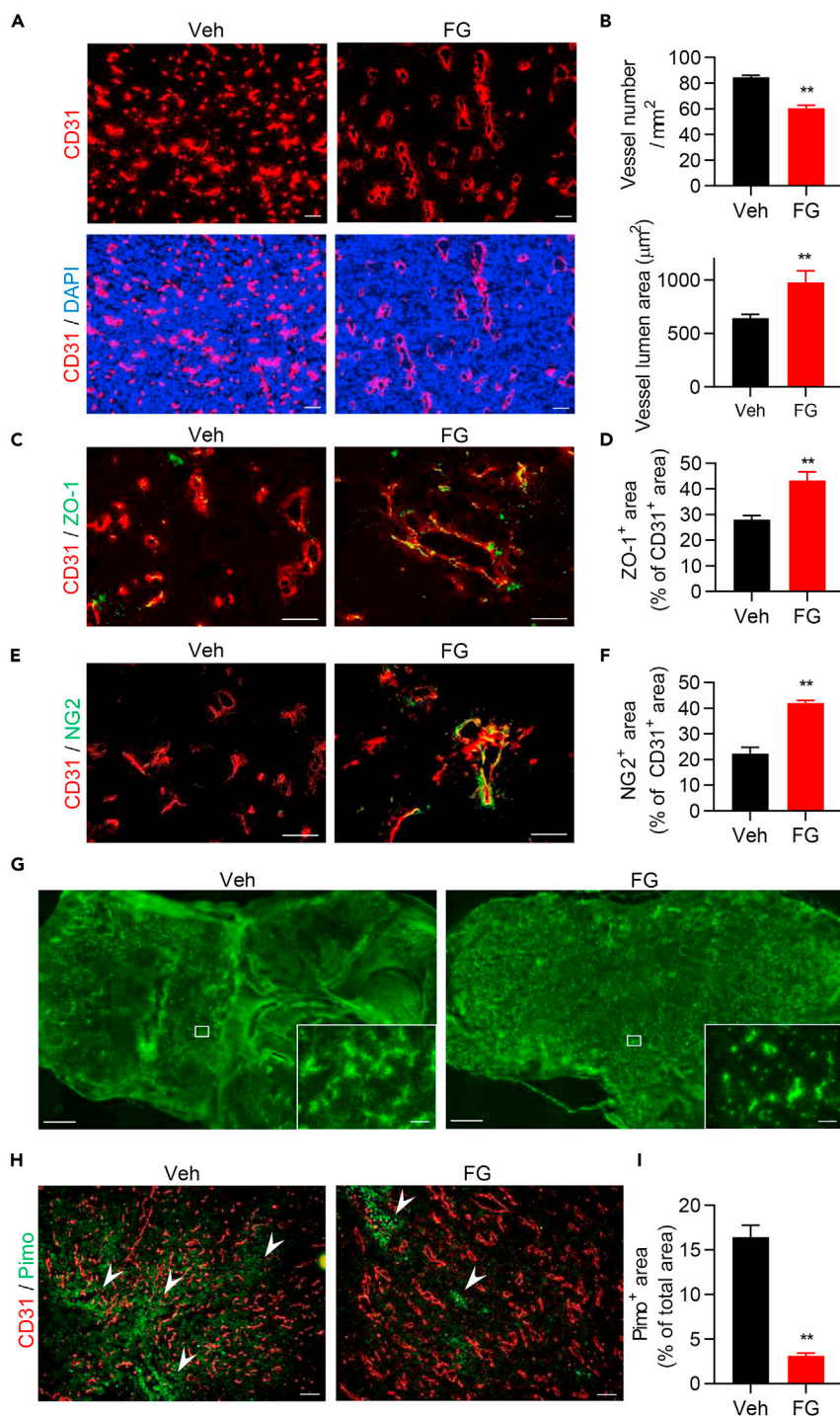
Figure 2. FG Treatment Improves TME

(A) IF images of CD31-stained (red) sections of LLC tumors. Scale bar, 100 μm.

(B) Quantification of vessel density and vessel lumen area in LLC tumors (n = 6).

(C) IF images of ZO-1 (green) and CD31 (red)-stained sections of LLC tumors. Scale bar, 50 μm.

(D) Quantification of the ZO-1$^+$ area ratio in the CD31$^+$ area (n = 5).

(E) IF images of NG2 (green) and CD31 (red)-stained sections of LLC tumors. Scale bar, 50 μm.

(F) Quantification of the NG2$^+$ area ratio in the CD31$^+$ area (n = 5).

Figure 2. *Continued*

(G) Images of blood perfusion (low-power field; scale bar, 1 mm) and blood leakage (high-power field; scale bar, 100 μm) in LLC tumor tissues using FITC-conjugated dextran.

(H and I) IF images and quantification of the tumor hypoxic region by anti-pimonidazole staining in LLC tumors (anti-CD31 antibody, red; anti-pimonidazole antibody, green; n = 6). Arrowheads indicate pimonidazole-positive area. Scale bar, 100 μm.

Data represent means ±SEM; Mann-Whitney test (B, D, F, and I). **p < 0.01. See also Figure S2.

analyzed other immune cell contents in circulating blood and tumor tissue and found no significant differences between vehicle and FG treatment (Figures S3E and S3F).

Further analysis was carried out on this tumor-infiltrating Mφ population, which would be polarized into M1 or M2 Mφs, by using CD80 as an M1 marker and CD206 as an M2 marker (Muller et al., 2017). However, these markers were expressed in both vehicle- and FG-treated tumor Mφs, and there were no differences between Mφs in either treatment group (Figure S3A). As recent studies demonstrated that TAMs simultaneously express both M1 and M2 markers (Azizi et al., 2018; Muller et al., 2017; Peterson et al., 2016), we focused on other cell surface markers, whose expression levels reflected the differentiated state of TAMs. Most TAM subpopulations arise from the Ly6C$^+$ population of circulating monocytes. Ly6C is downregulated during the differentiation of monocytes into TAMs (Franklin et al., 2014); however, there have been few reports on how the functions differ when TAMs are subdivided by Ly6C. Therefore, we divided these tumor-infiltrating Mφs using Ly6C into three populations, Ly6C^{hi}, Ly6C^{lo}, and Ly6C^{neg} (Figure S3A). The Ly6C^{lo} Mφ ratio in the total Mφ population increased by FG treatment (Figure 3F). Moreover, the morphology of Ly6C^{lo} Mφs from FG-treated tumors was different from Ly6C^{lo} Mφs from vehicle-treated tumors (Figure S3B). It is possible that these Mφs formed phagosomes.

We also analyzed tumor-infiltrating immune cells in the B16F10 and MC38 tumor models. The ratio of Ly6C Mφ fractions in the B16F10 tumor showed a similar tendency as the LLC mouse tumor-infiltrating Mφs (Figures 3G and 3H). However, the ratio of tumor-infiltrating Ly6C Mφ fractions in the MC38 tumor, in which no significant difference in tumor growth occurred after FG treatment, was different than that of the LLC and B16F10 tumors (Figures S3G and S3H). T cell infiltration to the tumor was lower in the LLC mouse model than in B16F10 and MC38 (Figures 3C, 3I, and S3I). In addition, T cells showed a slightly activated profile in the tumor tissues (Figure S3K) and circulating blood (Figure S3M) of B16F10 tumor-bearing mice after FG treatment compared with that of the LLC mouse model (Figures S3J and S3L). Therefore, we selected the LLC mouse model for further experiments to focus on tumor-infiltrating Mφs.

Among the three different tumor inoculation models, vascular normalization by FG was qualitatively similar, whereas tumor growth inhibition by FG was evident in the LLC model and B16F10 model but not in the MC38 model. Such differences may arise from the population of infiltrating Mφs. Therefore, we examined whether FG affected the ability of tumor-infiltrating Mφs to inhibit tumor growth. To test this, tumor-infiltrating Mφs were depleted by liposome clodronate before FG administration. Liposome control and FG-treated tumors showed inhibited tumor growth compared with that of vehicle-treated tumors. However, tumor growth was not significantly different between the vehicle- and FG-treated tumors in the clodronate treatment group (Figure 3J). Mφ depletion efficiency was evaluated by immunostaining; Mφs showed an approximate 80% depletion compared with that in liposome control tumor tissues and spleen (Figures 3K, 3L, and S3N). These results indicate that FG affects the ability of tumor-infiltrating Mφs to inhibit tumor growth.

FG Treatment Inhibits Tumor Growth through Mφs via the PHD-HIF Axis

PHD inhibitors impair prolyl hydroxylation and proteasome degradation of HIFs, which results in upregulation of the HIF signaling pathway (Hoppe et al., 2016). Therefore, we examined whether the FG-induced inhibition of tumor growth resulted from inhibition of the PHD-HIF axis. To genetically mimic the FG drug reaction, Mφ-specific Von Hippel Lindau (VHL)-knockout mice (VHL$^{fl/fl}$ LysM-Cre) were employed; VHL$^{fl/fl}$ LysM-Cre exhibits HIF upregulation (Kaelin, 2008). An LLC tumor transplantation model of VHL$^{fl/fl}$ LysM-Cre mice exhibited similar results as the FG-treated LLC tumor transplant mouse model, namely, tumor growth inhibition (Figures 4A–4C). Furthermore, the Ly6C^{lo} Mφ ratio in the total tumor-infiltrating Mφ
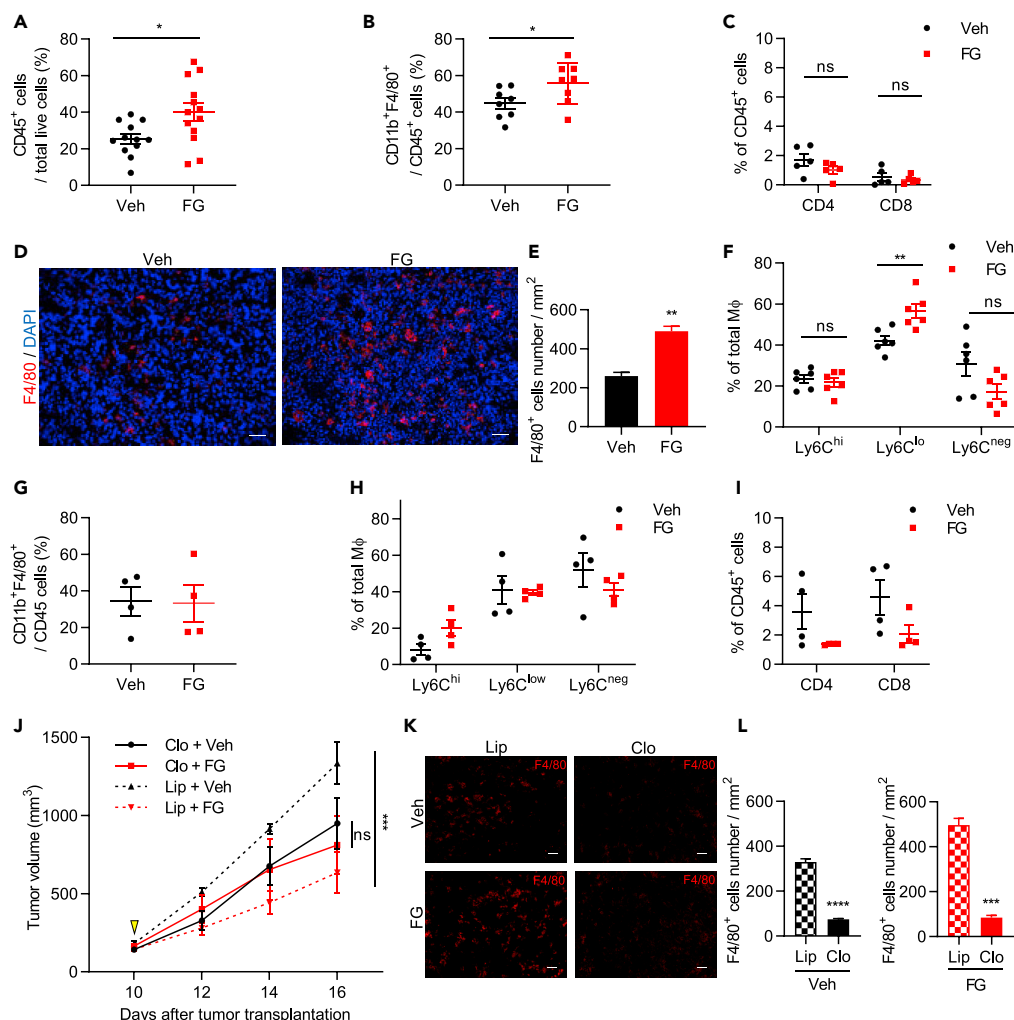
Figure 3. FG Treatment Induces Mφ Infiltration in Tumors and Inhibits Tumor Growth through Mφs

(A–C) Quantification of tumor-infiltrating (A) CD45+ (n = 12–13), (B) CD11b+F4/80+ (n = 8), and (C) CD4+ and CD8+ (n = 5) cell ratios in LLC tumors by flow cytometric analysis.

(D) IF imaging of F4/80 (red)-stained sections of LLC tumors. Scale bar, 50 μm.

(E) Quantification of F4/80+ cell number per mm² of tumors (n = 5).

(F–I) Flow cytometric quantification of (F) Ly6C^{hi}, Ly6C^{lo}, and Ly6C^{neg} Mφ ratios in LLC tumors (n = 6), (G) the ratio of tumor-infiltrating CD11b+F4/80+ cells/CD45+ cells in B16F10 tumors (n = 4), (H) Ly6C^{hi}, Ly6C^{lo}, and Ly6C^{neg} Mφs ratios in B16F10 tumors (n = 4), and (I) CD4+ and CD8+ cell lymphocyte ratios in B16F10 tumors (n = 4).

(J) Tumor growth curves of the LLC tumor mouse model treated with liposome control or clodronate liposome and vehicle or 3 mg FG (relative to vehicle liposome controls; n = 4).

(K) IF images of F4/80 (red)-stained sections of LLC tumors. Scale bar, 50 μm.

(L) Quantification of F4/80+ cell number per mm² of tumors (n = 3).

Data represent means ±SEM. Mann-Whitney test (A–C and E–I); two-way ANOVA (J); unpaired Student's t test (L). ns, not significant; *p < 0.05; **p < 0.01; ***p < 0.001; ****p < 0.0001. See also Figure S3.

population was increased in VHL$^{fl/fl}$ LysM-Cre mice (Figure 4D). Vessel density was also reduced, and the vessel lumen was found extended (Figures S4A and S4B). To examine the off-target effects of FG, an LLC tumor transplantation model of VHL$^{fl/fl}$ and VHL$^{fl/fl}$ LysM-Cre mice were treated with/without FG. In VHL$^{fl/fl}$ mice, FG treatment inhibited tumor growth compared with that of vehicle control (Figures S4C and S4D). However, no significant difference was observed in tumor growth between vehicle- and FG-treated tumors of VHL$^{fl/fl}$ LysM-Cre mice (Figures 4E, 4F, and S4E). Therefore, these results suggest that FG can inhibit tumor growth through Mφs via the PHD-HIF axis. To evaluate the effects of the PHD inhibitor on Mφs, we performed qPCR analysis of bone marrow-derived Mφs (BMDMs) and found that FG-treated
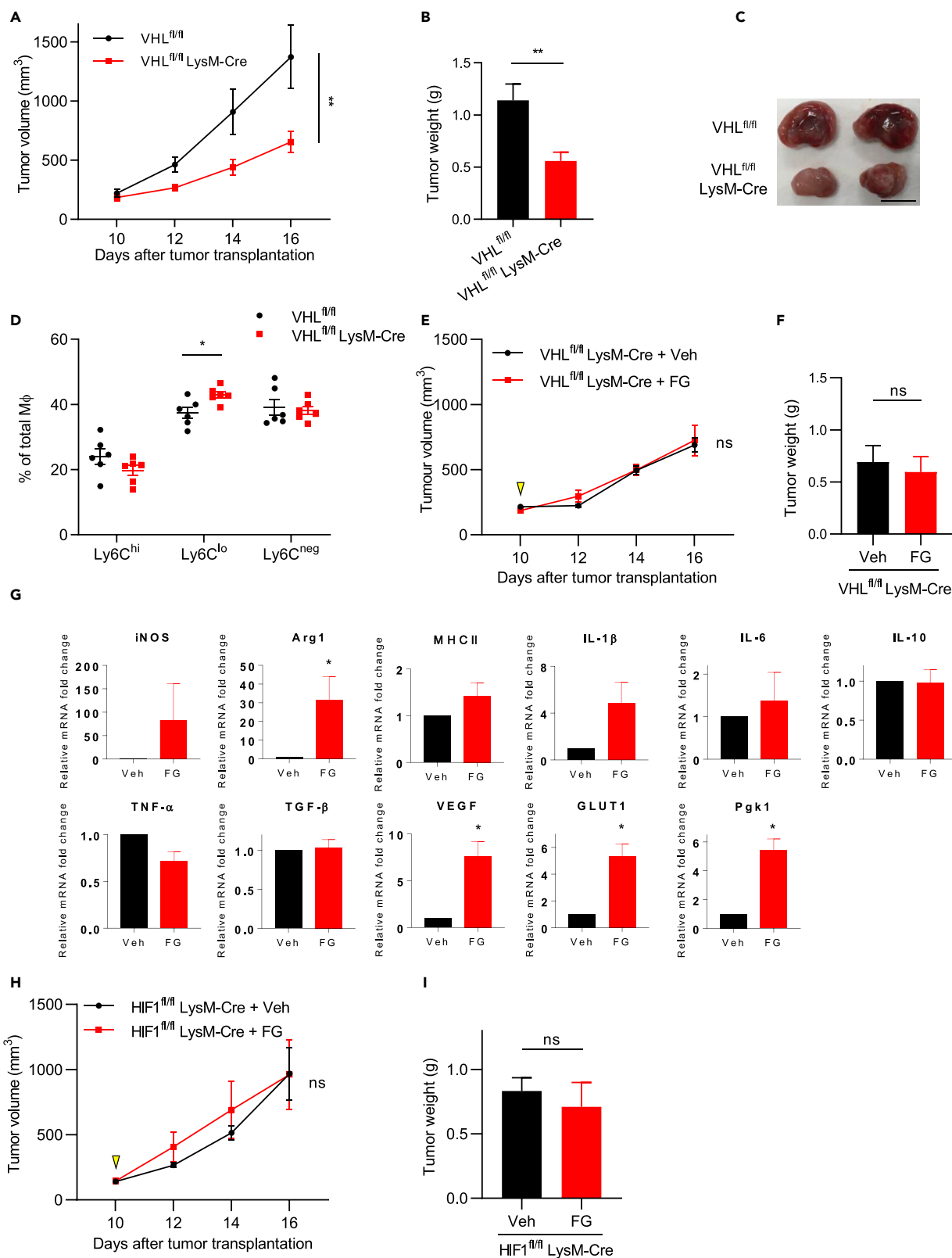
Figure 4. FG Treatment Inhibits Tumor Growth through Mφs via the PHD-HIF Axis

(A) Tumor growth curves of the LLC tumor model of *Vhl^fl/fl LysM-Cre^−/−* (VHL^fl/fl; n = 9) or *Vhl^fl/fl LysM-Cre^+/-* (VHL^fl/flLysM-Cre; n = 7) mice.

(B) Tumor weight on day 16 (n = 7–9).

(C) Images of tumors on day 16. Scale bar, 1 cm.

(D) Flow cytometric analysis of Ly6C^hi, Ly6C^lo, and Ly6C^neg Mφ ratios in the LLC tumor model (n = 6).

(E) Tumor growth curves of the LLC tumor model of *Vhl^fl/fl LysM-Cre^+/-* (VHL^fl/flLysM-Cre) mice. Treatment with Veh or FG (3 mg; treated on day 10); n = 3–4.

(F) Tumor weight on day 16 (n = 3–4).

(G) qPCR analysis of bone marrow-derived macrophages (BMDMs) treated with/without FG.

(H) Tumor growth curves of the LLC tumor model of *HIF-1^fl/fl LysM-Cre^+/-* (HIF1^fl/flLysM-Cre) mice. Treatment with Veh or FG (3 mg; treated on day 10); n = 4.

(I) Tumor weight on day 16 (n = 4).

Data represent means ± SEM; two-way ANOVA (A, E, and H); Mann-Whitney test (B, D, F, and I); paired t test (G). ns, not significant; *p < 0.05; **p < 0.01. See also Figure S4.

BMDMs showed upregulated HIF downstream gene expression (Figure 4G). Previous studies have demonstrated that HIF-1 participates in the M1 polarization of Mφs in an infectious mice model (Andrejeva and Rathmell, 2017; Semba et al., 2016). To assess this in a tumor model, Mφ-specific HIF-1-knockout mice (HIF1^fl/fl LysM-Cre) were employed. In HIF1^fl/fl mice, FG treatment inhibited tumor growth compared with that of vehicle treatment (Figures S4F and S4G). However, tumor growth was not significantly different between the vehicle- and FG-treated tumors of HIF1^fl/fl LysM-Cre mice (Figures 4H, 4I, and S4H). Taken together, these results indicate that the PHD inhibitor affects the HIF signaling pathway, especially the HIF-1 signaling pathway, in Mφs.

FG Directly Activates Phagocytosis in Mφs

Mφs play an important role in the innate immune system by directly inhibiting tumor growth through phagocytosis (Fiumara et al., 1997; Guerriero et al., 2017; Ubil et al., 2018). Therefore, we hypothesized that FG treatment induces Mφs to activate phagocytosis and thereby inhibit tumor growth. To examine Mφ-engulfed tumor cells in the FG-treated tumor tissue, we used the GFP-labeled LLC tumor model and harvested tumors 48 h after FG administration; these FG-treated tumors did not show normalized tumor vessels (Figures S2I and S2J) and there was a significant increase in tumor-phagocytic Mφs (GFP^+ Mφs; Figures 5A and 5B). Furthermore, we did not observe significant differences in cleaved caspase-3 and Ki-67 expression between vehicle and FG-treated tumors (Figures 1I–1L). Taking these results into consideration, we theorized that tumor growth was not inhibited because of apoptosis but possibly because of phagocytosis due to an increased number of phagocytic Mφs within the tumor.

To further verify the direct effects of FG on Mφs, a phagocytosis assay was performed using BMDMs *in vitro* (Figure 5C). The level of phagocytic Mφs increased in BMDMs treated with FG (Figures 5D and 5E). In addition, we cocultured BMDM and LLC *in vitro* and found that the phagocytic ability of tumor cells in BMDMs was activated by FG treatment (Figures 5F and 5G). Activated BMDMs continuously engulfed LLC cells (Figure S5A). Therefore, our results indicate that FG directly affects Mφs.

Next, we analyzed the duration of these FG direct effects on Mφs. We changed the culture medium 12 h after adding FG and then evaluated phagocytic activity 5 days later (Figure S5B). The phagocytic activity of Mφs observed following FG administration was absent by day 5 (Figures S5C and S5D), indicating that the direct effects of FG on Mφs were lost at least 5 days later. We also harvested GFP-labeled LLC tumors 7 days after FG treatment (on day 16) when the TME had improved and then examined the tumors for tumor-phagocytic Mφs *in vivo*. The increase in tumor-phagocytic Mφs was maintained in-FG treated tumor tissues (Figures S5E and S5F). Thus, these results imply that TME improvement prolongs the antitumor effects of Mφs.

To determine which Ly6C Mφ populations activate tumor phagocytosis after FG treatment, we analyzed GFP^+ Mφs levels, which were subdivided by Ly6C (Figure S5G). The ratio of GFP^+ Mφs in the Ly6C-positive population (Ly6C^hi and Ly6C^lo) were found increased on day 16 (Figures S5H). To further test this, three separate fractions of Mφs (Ly6C^hi, Ly6C^lo, and Ly6C^neg Mφs) were sorted from tumor tissues on day 16, and a phagocytosis assay was performed *ex vivo* (Figures 5H and S5I). Ly6C^lo Mφs sorted from FG-treated tumors showed a significantly higher ratio of phagocytic Mφs than that of Ly6C^lo Mφs sorted from vehicle-treated tumors (Figures 5I and 5J). The Ly6C^hi Mφ populations had a high ratio of phagocytic Mφs in both groups and there were no significant differences between them, but there was a similar tendency toward
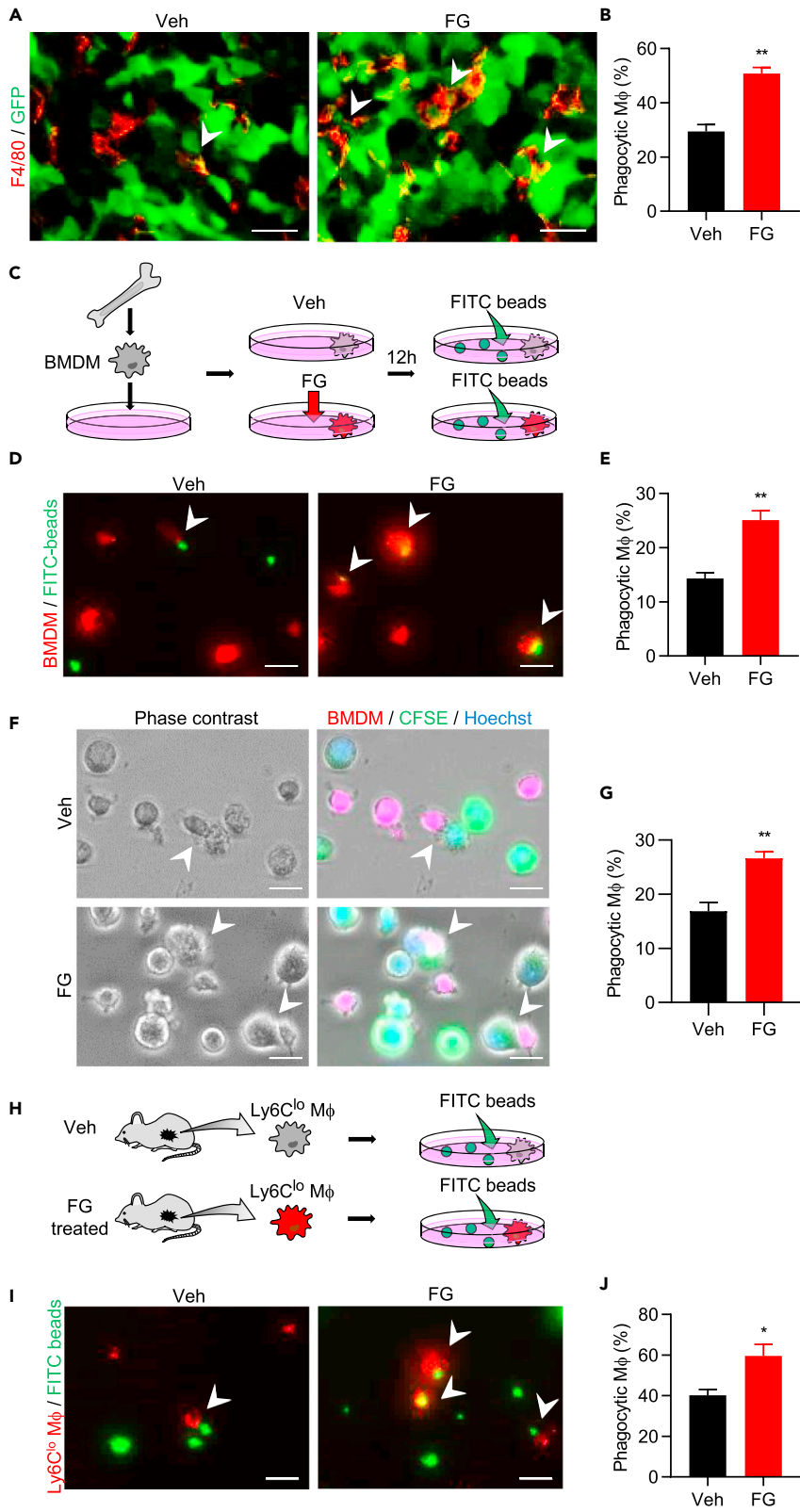
Figure 5. FG Directly Activates Phagocytosis in Mφs

(A) IF images of tumor-phagocytic Mφs. Tumor sections were stained with anti-GFP antibody (green) and anti-F4/80 antibody (red). Arrowheads indicate GFP$^+$F4/80$^+$ cells. Scale bar, 20 μm.

(B) Quantification of phagocytic (GFP$^+$F4/80$^+$) cell number in tumors (n = 5).

(C) Schematic diagram of the *in vitro* bead phagocytosis assay.

(D) Images of the *in vitro* BMDM bead phagocytosis assay. BMDMs were stained with CellVue Claret reagent (red); FITC-beads are shown in green. Arrowheads indicate phagocytic Mφs. Scale bar, 20 μm.

(E) Quantification of the phagocytic BMDM ratio. Three independent experiments were performed with two replicates.

(F) Images of the *in vitro* BMDM and LLC cell phagocytosis assay. BMDMs were stained with CellVue Claret reagent (red); LLC cells were stained with CFSE (green) and Hoechst (blue). Arrowheads indicate phagocytic Mφs. Scale bar, 20 μm.

(G) Quantification of the phagocytic BMDM ratio. Three independent experiments were performed.

(H) Schematic diagram of the *ex vivo* bead phagocytosis assay.

(I) Image of the *ex vivo* phagocytosis assay. Ly6C^{lo} Mφs were stained with CellVue Claret reagent (red); FITC-beads shown in green. Arrowheads indicate phagocytic Mφs. Scale bar, 20 μm.

(J) Quantification of the phagocytic Ly6C^{lo} Mφ ratio (n = 5).

Data represent means ± SEM. Statistical analysis was performed using the Mann–Whitney test. $*p < 0.05$; $**p < 0.01$. See also Figure S5.

increased phagocytosis as in the Ly6C^{lo} Mφ population after FG treatment (Figures S5J and S5K). Meanwhile, the Ly6C^{neg} Mφ populations showed no difference in tumor phagocytosis between those sorted from vehicle- and FG-treated tumors (Figures S5L and S5M). These data suggest that FG activates the tumor-phagocytic ability of Ly6C^{lo} Mφs.

Activation of Mφs via FG Treatment Inhibits Tumor Growth

To examine whether activation of Mφs by FG treatment inhibits tumor growth in a mouse model, Mφs were sorted from vehicle- or FG-treated tumors on day 16. Sorted Mφs were transplanted into day 10 tumor-bearing mice into the tumor locus (Figure 6A). Histological identification of transplanted macrophages indicated that the transplanted cells were widely distributed within the tumor (Figure S6A). Surprisingly, Ly6C^{lo} Mφs from mice subjected to FG-treated tumor transplantation showed inhibited tumor growth (Figures 6B–6D). We also performed the same experiment for Ly6C^{neg} Mφs from vehicle- and FG-treated tumors. Both Ly6C^{neg} Mφ-transplanted tumors showed no significant difference in tumor growth (Figures S6B and S6C). Interestingly, these Mφ-transplanted tumors induced changes to the vessel structure; specifically, tumor vessel density was significantly decreased, whereas the vessel luminal area increased (Figures S6D–S6F). Furthermore, ZO-1 and NG2 expression was significantly increased in Ly6C^{neg} Mφ-transplanted tumors (Figures S6G–S6J). These findings suggest that the Ly6C^{neg} Mφ population contributes to tumor vessel normalization.

Next, we examined whether Ly6C^{lo} Mφs, which were isolated from vehicle tumors and exposed *in vitro* to FG, could inhibit tumor growth in the tumor mouse model. Ly6C^{lo} Mφs sorted from vehicle-treated tumors were cultured with/without FG for 12 h and transplanted into tumor-bearing mice in the tumor locus (Figure 6E). FG-treated Ly6C^{lo} Mφ-transplanted tumors showed significantly inhibited tumor growth (Figures 6F–6H). Thus, our results demonstrate that FG directly affects Ly6C^{lo} Mφs and induces their activation, thereby inhibiting tumor growth.

DISCUSSION

In this study, we demonstrated that FG treatment inhibits tumor growth by activating tumor-infiltrating Mφs and normalizing tumor vessels via the PHD-HIF axis. We also characterized the tumor-infiltrating Mφ population into three types, Ly6C^{lo}, Ly6C^{neg}, and Ly6C^{hi}.

The Ly6C^{lo} Mφ population showed the most drastic change in phenotype after FG treatment. Tumor growth inhibition by FG was observed in the LLC and B16F10 tumor models, but the MC38 tumor model, which contained fewer Ly6C^{lo} Mφs, did not show tumor growth inhibition following FG treatment. A recent study showed that Ly6C^{lo} Mφs along the tumor margins can prevent cytotoxic lymphocyte infiltration into the tumor core (Beatty et al., 2015). The lower the activity of cytotoxic lymphocytes in the tumor, the higher the malignancy of the tumor; consequently, the rate of tumor growth is thought to be faster (Fridman et al., 2012). In fact, LLC and B16F10 tumors had a higher rate of tumor growth than did MC38 in this study. Taking these factors into consideration, the Ly6C^{lo} Mφ population may contribute to tumor growth. More importantly, our results showed that FG treatment can alter the Ly6C^{lo} Mφ phenotype to a phagocytic phenotype, which would show activity against the tumor.
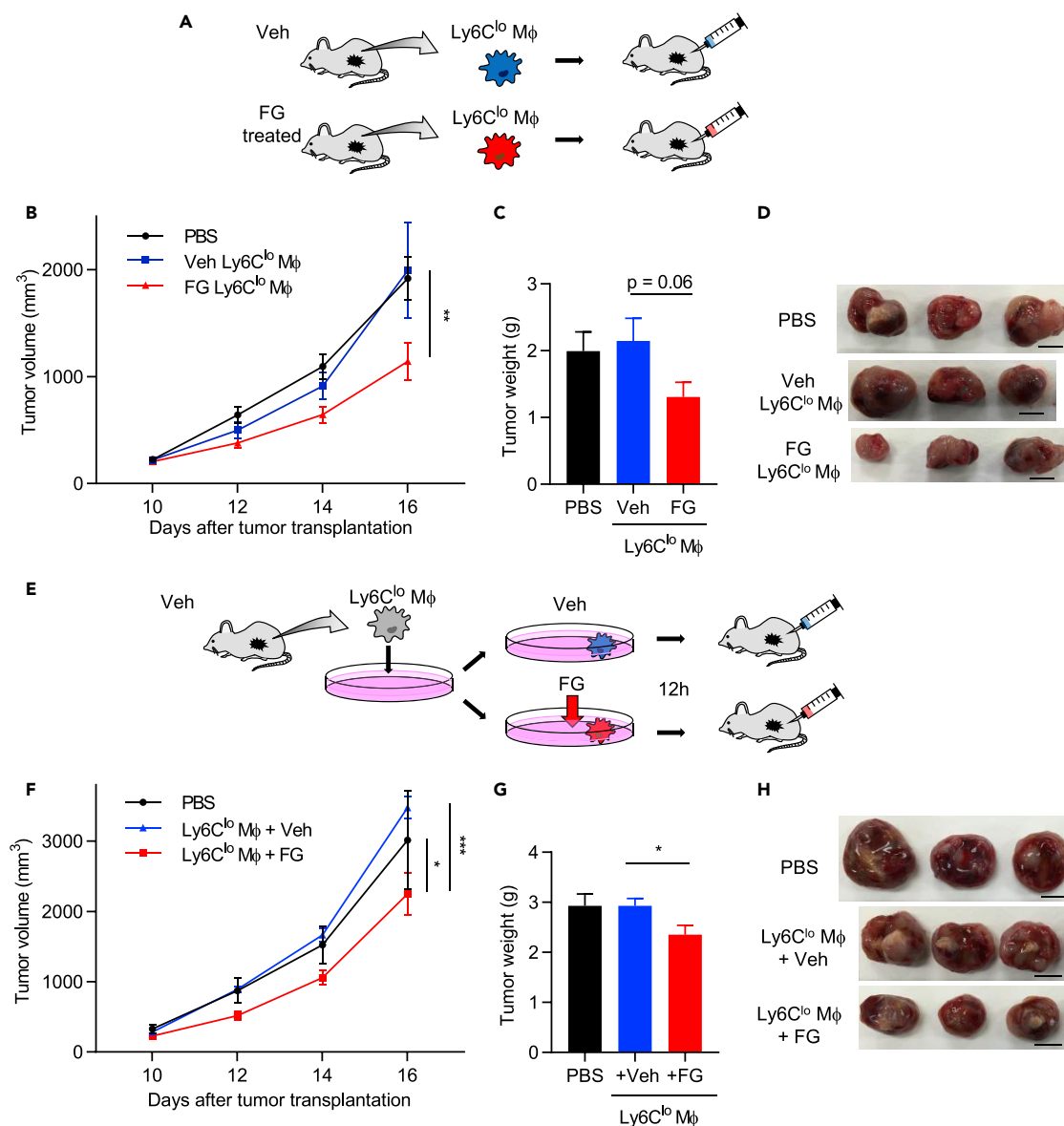
Figure 6. Activation of Mφs via FG Treatment Inhibits Tumor Growth

(A) Schematic diagram of sorted Ly6C^{lo} Mφs transplanted into the tumor locus.

(B) Tumor growth curves of the LLC tumor mouse models with PBS-injected or transplanted Ly6C^{lo} Mφs from vehicle- or FG-treated mouse tumors (n = 6). **p < 0.01 vs. PBS and Veh Ly6C^{lo} Mφ (two-way ANOVA).

(C) Tumor weight on day 16 (n = 6). *p = 0.06 (Mann-Whitney test).

(D) Images of the tumor on day 16. Scale bar, 1 cm.

(E) Schematic diagram of sorted Ly6C^{lo} Mφ transplantation; cells were treated with/without FG before transplantation into the tumor locus.

(F) Tumor growth curves of LLC tumor mouse models with PBS-injected or transplanted FG treated with/without Ly6C^{lo} Mφs on day 10 (n = 5). *p < 0.05 vs. PBS; ***p < 0.001 vs. Ly6C^{lo} Mφ + Veh (two-way ANOVA).

(G) Tumor weight on day 16 (n = 5). *p < 0.05 versus Ly6C^{lo} Mφ + Veh (unpaired Student's t test).

(H) Images of the LLC tumor on day 16. Scale bar, 1 cm.

Data represent means ± SEM. See also Figure S6.

We further found that Ly6C^{neg} Mφs may be associated with tumor vessel normalization. When Ly6C^{neg} Mφs were transplanted into tumors, tumor-infiltrating Mφs isolated from both vehicle- and FG-treated tumors altered tumor vessel structure. In addition, vessel formation was strongly induced in Ly6C^{neg} Mφs isolated

from FG-treated tumors. These findings suggest that FG treatment also affects Ly6C^{neg} Mφ, leading to tumor vessel normalization.

Ly6C[hi] Mφs isolated from vehicle-treated tumors exhibited higher phagocytic ability than that of the Ly6C^{lo} and Ly6C^{neg} Mφ populations *in vitro*. Furthermore, our results showed that FG may also activate the phagocytic ability of Ly6C^{hi} Mφs. Unfortunately, owing to their fragile expanded cell structure after engulfing tumor cells, it was too difficult to purify and isolate live Ly6C^{hi} Mφs from tumors in the transplantation experiment.

Recent studies demonstrated that TAMs simultaneously express both M1 and M2 markers (Azizi et al., 2018; Muller et al., 2017; Peterson et al., 2016). In this study we used CD80 as an M1 cell surface marker and CD206 as an M2 cell surface marker. Consistent with recent reports, these markers were expressed in both vehicle- and FG-treated tumor-infiltrating Mφs, and there were no differences. We analyzed other cell surface markers, such as MHCII, but we were unable to observe any changes in expression after FG treatment. Furthermore, we examined gene expression levels in BMDMs treated with/without FG. FG-treated BMDMs showed upregulation of HIF downstream gene expression (VEGF, GLUT1, etc.) as well as M1 marker genes (iNOS, MHCII, IL-1β, IL-6, and TNF-α) and M2 marker genes (Arginase-1 and IL-10). Thus, it was too difficult to distinguish and determine Mφ polarization using existing markers. The mixed phenotype of Mφs, which consists of the inflammatory (M1) and anti-inflammatory (M2) phenotypes, may depend on the balance of each molecule.

A previous study demonstrated that heterozygous deficiency of *Phd2* in endothelial cells does not affect vessel lumen size but normalizes the endothelial barrier and pericyte coverage (Leite de Oliveira et al., 2012). Most of our results are in agreement with previous reports, but one thing was different; the vessel lumen area was found increased in this study. We previously showed that the PHD inhibitor elongates tumor vessel diameter (Koyama et al., 2017) and suggested that the tumor vessels were reconstituted after PHD inhibitor treatment. This may have resulted from PHD inhibitor treatment, which affects not only endothelial cells but also Mφs and other cells.

Several studies have previously reported that tumor vessel normalization either did not changed the tumor size (Cantelmo et al., 2016; Mazzone et al., 2009) or increased tumor size along with change in apoptosis and/or proliferation (Folkman,1971; Krzywinska et al., 2017). On the other hand, other studies have reported that vessel normalization alters the TME and activates anti-tumor immunity; therefore, vascular normalization is emerging as a strategy for enhancing cancer therapy (Quail and Joyce, 2013; Henze and Mazzone, 2016; Park et al., 2016). In the present study, the expression levels of the apoptosis marker, cleaved caspase-3, and the proliferation marker, Ki-67, did not change in the FG-treated tumors. FG treatment not only led to normalization of tumor vessels and improved the TME but also directly activated phagocytosis in Mφs. In addition, several studies have reported that Mφs play an important role in the innate immune system by directly inhibiting tumor growth through phagocytosis without inducing apoptosis (Fiumara et al., 1997; Guerriero et al., 2017; Ubil et al., 2018). Therefore, we argue that the tumor growth inhibition in FG-treated tumors is contributed by phagocytosis due to an increased number of phagocytic Mφs within the tumor.

HIF stabilization in CD8^{+} T cells results in increased expression and release of important cytolytic molecules, such as granzyme B and perforin (Doedens et al., 2010; Palazon et al., 2014, 2017). This suggests that T cells function in tumor growth inhibition. Consistent with this, we observed that T cells were slightly activated in B16F10 tumor tissues and circulating blood of B16F10 tumor-bearing mice after FG treatment. Therefore, in the B16F10 tumor model, FG may affect not only tumor-infiltrating Mφs but also T cells. However, unexpectedly, T cell activation was not observed in the LLC tumor model and Mφs were the primary factors after FG treatment. Further studies are needed to elucidate the role of the PHD-inhibitor on T cells.

We have previously shown that the PHD-HIF axis induces angiogenesis and promotes tissue wound healing (Koyama et al., 2017; Takaku et al., 2012). In the present study, we used *Vhl LysM Cre* mice to confirm the main working mechanism of FG. VHL was associated with prolyl hydroxylated HIFs and promoted HIF degradation (Kaelin, 2008; Takeda et al., 2010). VHL^{fl/fl} LysM-Cre mice showed a similar phenotype as the FG-treated tumor, where tumor growth was inhibited, the Ly6C^{lo} Mφ ratio in the total tumor-infiltrating Mφs increased, and tumor vessels were normalized. Thus, the PHD inhibitor may affect not only endothelial cells but also tumor-infiltrating Mφs via the PHD-HIF axis. Moreover, HIF-1α drives a metabolic shift toward

glycolysis and is associated with M1 polarization in an infectious mice model (Semba et al., 2016). In this study, we showed that tumor growth was not significantly different between vehicle- and FG-treated tumors in HIF-1$^{fl/fl}$LysMCre mice, suggesting that HIF-1 may polarize Mφs to an M1-like phenotype even in tumor-infiltrating Mφs. Therefore, tumor-infiltrating Mφs may change their phenotypes to that of anti-tumor Mφs via the PHD-HIF axis after treatment with the PHD inhibitor.

In this study, we showed that FG inhibits the growth of tumors that are TAM abundant and contain few activated T cells in a subcutaneous tumor model. This tumor immune microenvironment is associated with tumor malignancy and results in therapeutic resistance (Binnewies et al., 2018). Therefore, we chose this subcutaneous tumor model to identify the therapeutic strategies against these tumors. However, our model does not completely reproduce the local TME. Tissue-resident Mφs respond to diverse environmental signals and have distinct global expression profiles (Lavin et al., 2014). Therefore, orthotopic or genetically engineered mouse models are important for reproducing the local TME and evaluating the effect of FG treatment on tissue-resident Mφs. However, we hope that our study may lead to the development of the therapeutic strategy against TAM-abundant tumors that contain few activated T cells.

In conclusion, we demonstrated that FG inhibits tumor growth by activating tumor-infiltrating Mφs and normalizing tumor vessels and the TME via the PHD-HIF axis. In particular, FG treatment altered the Ly6C^{lo} Mφs phenotype, which is associated with tumor malignancy, to an anti-tumor phenotype. Therefore, the PHD inhibitor can potentially be utilized for promoting the anti-tumor potential of Mφs to improve cancer therapy.

Limitations of the Study

In this study, we showed that FG treatment inhibited tumor growth by activating the phagocytic ability of tumor-infiltrating Mφs via the PHD-HIF axis. However, we were unable to analyze the gene expression of activated tumor-infiltrating Mφs *in vivo*. This is because activated tumor-infiltrating Mφs had already engulfed LLC cells, and thus any internal controls were unsuccessful. Therefore, we alternatively examined changes in gene expression using FG-treated BMDMs. We are working on analyzing gene expression changes of activated tumor-infiltrating Mφs after FG treatment for future studies. In addition, we chose a subcutaneous tumor injection model because we wanted to assess the effect of FG treatment on tumors that are TAM abundant and contain few activated T cells. Orthotopic or genetically engineered mouse models would be needed to precisely reproduce the local TME and evaluate the effects of FG on tissue-resident Mφs.

METHODS

All methods can be found in the accompanying Transparent Methods supplemental file.

SUPPLEMENTAL INFORMATION

Supplemental Information can be found online at https://doi.org/10.1016/j.isci.2019.08.033.

AUTHOR CONTRIBUTIONS

S.N. and S.M. performed the majority of the experiments and data analysis. M.S. performed the gene editing experiment. T.Y. and S.K. performed the mice breeding and histological experiments. N.T. performed part of the VHL$^{f/f}$ LysM-Cre mice experiments. M.T. performed part of the MC38 transplant experiments. S.N., S.M., M.S., K.M., and S.T. designed experiments. S.N., S.M., M.S., T.Y., S.K., N.T., M.T., Y.M., J.U., T.N., K.M., and S.T. interpreted the data and provided necessary materials. S.N., S.M., and S.T. drafted the manuscript. S.M. and S.T. conceived the concept of the study and supervised the research. All authors reviewed the manuscript.

iScience

CellPress

DECLARATION OF INTERESTS

The authors declare no competing interests.

REFERENCES

Andrejeva, G., and Rathmell, J.C. (2017). Similarities and distinctions of cancer and immune metabolism in inflammation and tumors. Cell Metab. *26*, 49–70.

Azizi, E., Carr, A.J., Plitas, G., Cornish, A.E., Konopacki, C., Prabhakaran, S., Nainys, J., Wu, K., Kiseliovas, V., Setty, M., et al. (2018). Single-cell map of diverse immune phenotypes in the breast tumor microenvironment. Cell *174*, 1293–1308.e36.

Beatty, G.L., Winograd, R., Evans, R.A., Long, K.B., Luque, S.L., Lee, J.W., Clendenin, C., Gladney, W.L., Knoblock, D.M., Guirnalda, P.D., et al. (2015). Exclusion of T cells from pancreatic carcinomas in mice is regulated by Ly6C(low) F4/80(+) extratumoral macrophages. Gastroenterology *149*, 201–210.

Besarab, A., Chernyavskaya, E., Motylev, I., Shutov, E., Kumbar, L.M., Gurevich, K., Chan, D.T., Leong, R., Poole, L., Zhong, M., et al. (2016). Roxadustat (FG-4592): Correction of anemia in incident dialysis patients. J. Am. Soc. Nephrol. *27*, 1225–1233.

Binnewies, M., Roberts, E.W., Kersten, K., Chan, V., Fearon, D.F., Merad, M., Coussens, L.M., Gabrilovich, D.I., Ostrand-Rosenberg, S., Hedrick, C.C., et al. (2018). Understanding the tumor immune microenvironment (TIME) for effective therapy. Nat. Med. *24*, 541–550.

Cantelmo, A.R., Conradi, L.C., Brajic, A., Goveia, J., Kalucka, J., Pircher, A., Chaturvedi, P., Hol, J., Thienpont, B., Teuwen, L.A., et al. (2016). Inhibition of the glycolytic activator PFKFB3 in endothelium induces tumor vessel normalization, impairs metastasis, and improves chemotherapy. Cancer Cell *30*, 968–985.

Doedens, A.L., Stockmann, C., Rubinstein, M.P., Liao, D., Zhang, N., DeNardo, D.G., Coussens, L.M., Karin, M., Goldrath, A.W., and Johnson, R.S. (2010). Macrophage expression of hypoxia-inducible factor-1 alpha suppresses T-cell function and promotes tumor progression. Cancer Res. *70*, 7465–7475.

Du, R., Lu, K.V., Petritsch, C., Liu, P., Ganss, R., Passegue, E., Song, H., Vandenberg, S., Johnson, R.S., Werb, Z., et al. (2008). HIF1alpha induces the recruitment of bone marrow-derived vascular modulatory cells to regulate tumor angiogenesis and invasion. Cancer Cell *13*, 206–220.

Fiumara, A., Belfiore, A., Russo, G., Salomone, E., Santonocito, G.M., Ippolito, O., Vigneri, R., and Gangemi, P. (1997). In situ evidence of neoplastic cell phagocytosis by macrophages in papillary thyroid cancer. J. Clin. Endocrinol. Metab. *82*, 1615–1620.

Folkman, J. (1971). Tumor angiogenesis: therapeutic implications. N. Engl. J. Med. *285*, 1182–1186.

Franklin, R.A., Liao, W., Sarkar, A., Kim, M.V., Bivona, M.R., Liu, K., Pamer, E.G., and Li, M.O. (2014). The cellular and molecular origin of tumor-associated macrophages. Science *344*, 921–925.

Fridman, W.H., Pages, F., Sautes-Fridman, C., and Galon, J. (2012). The immune contexture in human tumours: impact on clinical outcome. Nat. Rev. Cancer *12*, 298–306.

Guerriero, J.L., Sotayo, A., Ponichtera, H.E., Castrillon, J.A., Pourzia, A.L., Schad, S., Johnson, S.F., Carrasco, R.D., Lazo, S., Bronson, R.T., et al. (2017). Class IIa HDAC inhibition reduces breast tumours and metastases through anti-tumour macrophages. Nature *543*, 428–432.

Henze, A.T., and Mazzone, M. (2016). The impact of hypoxia on tumor-associated macrophages. J. Clin. Invest. *126*, 3672–3679.

Hoppe, G., Yoon, S., Gopalan, B., Savage, A.R., Brown, R., Case, K., Vasanji, A., Chan, E.R., Silver, R.B., and Sears, J.E. (2016). Comparative systems pharmacology of HIF stabilization in the prevention of retinopathy of prematurity. Proc. Natl. Acad. Sci. U S A *113*, E2516–E2525.

Imtiyaz, H.Z., and Simon, M.C. (2010). Hypoxia-inducible factors as essential regulators of inflammation. Curr. Top. Microbiol. Immunol. *345*, 105–120.

Jain, R.K. (2014). Antiangiogenesis strategies revisited: from starving tumors to alleviating hypoxia. Cancer Cell *26*, 605–622.

Kaelin, W.G., Jr. (2008). The von Hippel-Lindau tumour suppressor protein: O2 sensing and cancer. Nat. Rev. Cancer *8*, 865–873.

Keith, B., Johnson, R.S., and Simon, M.C. (2011). HIF1alpha and HIF2alpha: sibling rivalry in hypoxic tumour growth and progression. Nat. Rev. Cancer *12*, 9–22.

Koyama, S., Matsunaga, S., Imanishi, M., Maekawa, Y., Kitano, H., Takeuchi, H., and Tomita, S. (2017). Tumour blood vessel normalisation by prolyl hydroxylase inhibitor repaired sensitivity to chemotherapy in a tumour mouse model. Sci. Rep. *7*, 45621.

Krzywinska, E., Kantari-Mimoun, C., Kerdiles, Y., Sobecki, M., Isagawa, T., Gotthardt, D., Castells, M., Haubold, J., Millien, C., Viel, T., et al. (2017). Loss of HIF-1alpha in natural killer cells inhibits tumour growth by stimulating non-productive angiogenesis. Nat. Commun. *8*, 1597.

Lavin, Y., Winter, D., Blecher-Gonen, R., David, E., Keren-Shaul, H., Merad, M., Jung, S., and Amit, I. (2014). Tissue-resident macrophage enhancer landscapes are shaped by the local microenvironment. Cell *159*, 1312–1326.

Leite de Oliveira, R., Deschoemaeker, S., Henze, A.T., Debackere, K., Finisguerra, V., Takeda, Y., Roncal, C., Dettori, D., Tack, E., Jonsson, Y., et al. (2012). Gene-targeting of Phd2 improves tumor response to chemotherapy and prevents side-toxicity. Cancer Cell *22*, 263–277.

Mazzone, M., Dettori, D., de Oliveira, R.L., Loges, S., Schmidt, T., Jonckx, B., Tian, Y.M., Lanahan, A.A., Pollard, P., de Almodovar, C.R., et al. (2009). Heterozygous deficiency of PHD2 restores tumor oxygenation and inhibits metastasis via endothelial normalization. Cell *136*, 839–851.

Mosser, D.M., and Edwards, J.P. (2008). Exploring the full spectrum of macrophage activation. Nat. Rev. Immunol. *8*, 958–969.

Movahedi, K., Laoui, D., Gysemans, C., Baeten, M., Stange, G., Van den Bossche, J., Mack, M., Pipeleers, D., In't Veld, P., De Baetselier, P., et al. (2010). Different tumor microenvironments contain functionally distinct subsets of macrophages derived from Ly6C(high) monocytes. Cancer Res. *70*, 5728–5739.

Muller, S., Kohanbash, G., Liu, S.J., Alvarado, B., Carrera, D., Bhaduri, A., Watchmaker, P.B., Yagnik, G., Di Lullo, E., Malatesta, M., et al. (2017). Single-cell profiling of human gliomas reveals macrophage ontogeny as a basis for regional differences in macrophage activation in the tumor microenvironment. Genome Biol. *18*, 234.

Nizet, V., and Johnson, R.S. (2009). Interdependence of hypoxic and innate immune responses. Nat. Rev. Immunol. *9*, 609–617.

Palazon, A., Goldrath, A.W., Nizet, V., and Johnson, R.S. (2014). HIF transcription factors, inflammation, and immunity. Immunity *41*, 518–528.

Palazon, A., Tyrakis, P.A., Macias, D., Velica, P., Rundqvist, H., Fitzpatrick, S., Vojnovic, N., Phan, A.T., Loman, N., Hedenfalk, I., et al. (2017). An HIF-1alpha/VEGF-A axis in cytotoxic T cells regulates tumor progression. Cancer Cell *32*, 669–683.e5.

Park, J.S., Kim, I.K., Han, S., Park, I., Kim, C., Bae, J., Oh, S.J., Lee, S., Kim, J.H., Woo, D.C., et al. (2016). Normalization of tumor vessels by Tie2 activation and Ang2 inhibition enhances drug delivery and produces a

favorable tumor microenvironment. Cancer Cell *30*, 953–967.

Peterson, T.E., Kirkpatrick, N.D., Huang, Y., Farrar, C.T., Marijt, K.A., Kloepper, J., Datta, M., Amoozgar, Z., Seano, G., Jung, K., et al. (2016). Dual inhibition of Ang-2 and VEGF receptors normalizes tumor vasculature and prolongs survival in glioblastoma by altering macrophages. Proc. Natl. Acad. Sci. U S A *113*, 4470–4475.

Provenzano, R., Besarab, A., Sun, C.H., Diamond, S.A., Durham, J.H., Cangiano, J.L., Aiello, J.R., Novak, J.E., Lee, T., Leong, R., et al. (2016). Oral hypoxia-inducible factor prolyl hydroxylase inhibitor roxadustat (FG-4592) for the treatment of anemia in patients with CKD. Clin. J. Am. Soc. Nephrol. *11*, 982–991.

Quail, D.F., and Joyce, J.A. (2013). Microenvironmental regulation of tumor progression and metastasis. Nat. Med. *19*, 1423–1437.

Semba, H., Takeda, N., Isagawa, T., Sugiura, Y., Honda, K., Wake, M., Miyazawa, H., Yamaguchi, Y., Miura, M., Jenkins, D.M., et al. (2016). HIF-1alpha-PDK1 axis-induced active glycolysis plays an essential role in macrophage migratory capacity. Nat. Commun. *7*, 11635.

Semenza, G.L. (2012). Hypoxia-inducible factors in physiology and medicine. Cell *148*, 399–408.

Stockmann, C., Doedens, A., Weidemann, A., Zhang, N., Takeda, N., Greenberg, J.I., Cheresh, D.A., and Johnson, R.S. (2008). Deletion of vascular endothelial growth factor in myeloid cells accelerates tumorigenesis. Nature *456*, 814–818.

Takaku, M., Tomita, S., Kurobe, H., Kihira, Y., Morimoto, A., Higashida, M., Ikeda, Y., Ushiyama, A., Hashimoto, I., Nakanishi, H., et al. (2012). Systemic preconditioning by a prolyl hydroxylase inhibitor promotes prevention of skin flap

necrosis via HIF-1-induced bone marrow-derived cells. PLoS One *7*, e42964.

Takeda, N., O'Dea, E.L., Doedens, A., Kim, J.W., Weidemann, A., Stockmann, C., Asagiri, M., Simon, M.C., Hoffmann, A., and Johnson, R.S. (2010). Differential activation and antagonistic function of HIF-α isoforms in macrophages are essential for NO homeostasis. Genes Dev. *24*, 491–501.

Tian, L., Goldstein, A., Wang, H., Ching Lo, H., Sun Kim, I., Welte, T., Sheng, K., Dobrolecki, L.E., Zhang, X., Putluri, N., et al. (2017). Mutual regulation of tumour vessel normalization and immunostimulatory reprogramming. Nature *544*, 250–254.

Ubil, E., Caskey, L., Holtzhausen, A., Hunter, D., Story, C., and Earp, H.S. (2018). Tumor-secreted Pros1 inhibits macrophage M1 polarization to reduce antitumor immune response. J. Clin. Invest. *128*, 2356–2369.

Supplemental Information

Controlling the Phenotype of Tumor-Infiltrating

Macrophages via the PHD-HIF Axis

Inhibits Tumor Growth in a Mouse Model

Shunji Nishide, Shinji Matsunaga, Masayuki Shiota, Takehiro Yamaguchi, Shojiro Kitajima, Yoichi Maekawa, Norihiko Takeda, Michio Tomura, Junji Uchida, Katsuyuki Miura, Tatsuya Nakatani, and Shuhei Tomita
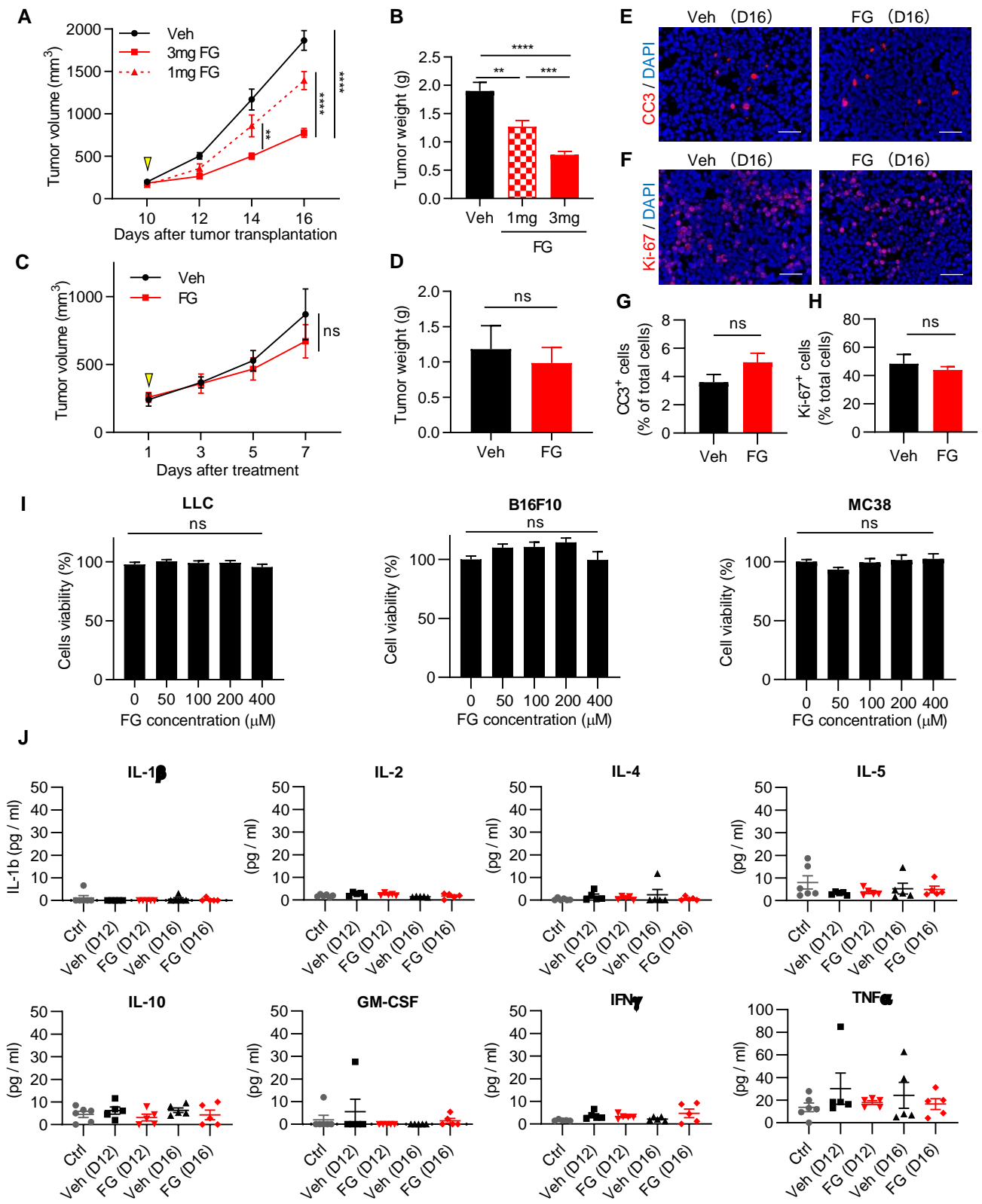
Figure S1. Effect of FG on tumor growth in LLC, B16F10, and MC38 tumor models. Related to Figure 1.

(A) Transplanted LLC (1×10^6 cells/mouse) tumor size in C57BL/6 mice was measured after treatment with vehicle (n = 15), 1 mg FG (n = 10), or 3 mg FG (n = 15) on day 10. **$p < 0.01$; ****$p < 0.0001$; two-way ANOVA. (B) Tumor weight was measured at the end of the experiment on day 16 (n = 10–15). **$p < 0.01$, ***$p < 0.001$, ****$p < 0.0001$; Mann-Whitney test. (C) Transplanted MC38 (1×10^6 cells/mouse) tumor size in C57BL/6 mice was measured after treatment with vehicle (n = 4) or 3 mg FG (n = 5) on day 10. ns, not significant; two-way ANOVA. (D) Tumor weight was measured at the end of the experiment on day 16 (n = 3–4). ns, not significant; Mann-Whitney test. (E) Immunofluorescence (IF) of cleaved caspase-3 (CC3; red)-stained sections of LLC tumors on day 16. Scale bar = 50 μm. (F) IF images of cleaved Ki-67 (red)-stained sections of LLC tumors on day 16. Scale bar = 50 μm. (G) Quantification of the CC3$^+$ cell ratio of total cells on day 16 (n = 5). ns, not significant; Mann-Whitney test. (H) Quantification of the Ki-67$^+$ cell ratio of total cells on day 16 (n = 3). ns, not significant; Mann-Whitney test. (I) Cell proliferation of LLC, B16F10, and MC38 cells were measured 72 h after FG treatment. ns, not significant vs. 0 μM, as determined by one-way ANOVA. Three independent experiments were performed in triplicate. (J) Blood plasma concentrations were determined via multiplex assays.

A Veh (D19)　　FG once (D19)　CD31

B Vessel number / mm² ns　Vessel lumen area (μm²) ns

C Veh (D23)　　FG twice (D23)　CD31

D Vessel number / mm² *　Vessel lumen area (μm²) *

E Veh　　FG　CD31

F Vessel number / mm² *　Vessel lumen area (μm²) *

G Veh　　FG　CD31

H Vessel number / mm² *　Vessel lumen area (μm²) *

I Veh (D12)　　FG once (D12)　CD31

J Vessel number / mm² ns　Vessel lumen area (μm²) ns
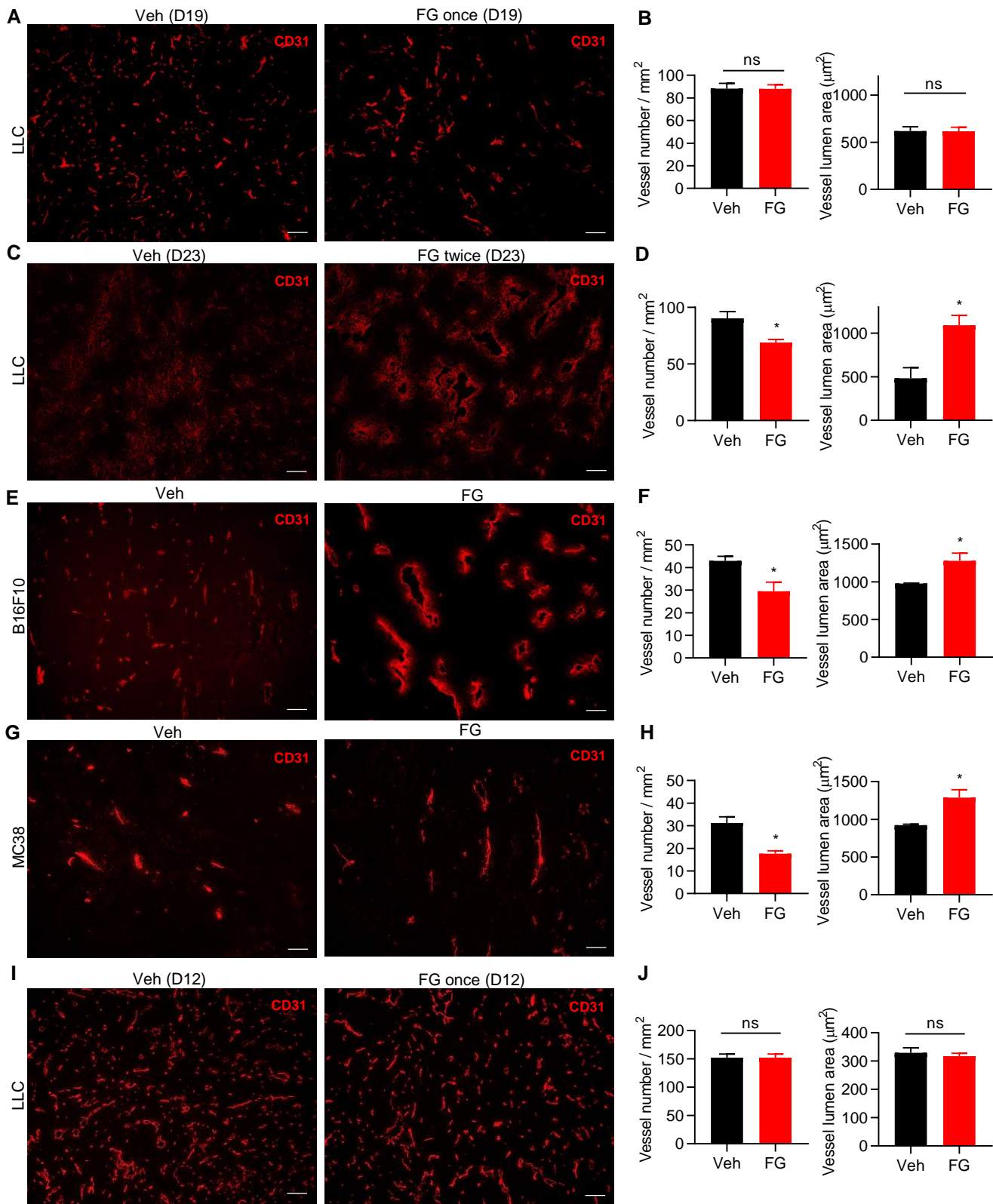
Figure S2.

Figure S2. Effect of FG on tumor vessels in LLC, B16F10, and MC38 tumor models. Related to Figure 2.

(A) Immunofluorescence (IF) images of CD31-stained sections of LLC tumors on day 19 from vehicle- and one-time FG-treated mice. (B) Quantification of vessel density and vessel lumen area in s.c. LLC tumors from vehicle- and FG-treated mice (n = 3). ns, not significant; unpaired Student's t-test. (C) IF images of CD31-stained sections of LLC tumors on day 23 from vehicle- and FG-treated (multiple times) mice. (D) Quantification of vessel density and vessel lumen area in s.c. LLC tumors of vehicle and FG-treated mice (n = 3). *p < 0.05; unpaired Student's t-test. (E) IF images of CD31-stained sections of B16F10 tumors on day 16 from vehicle- and FG-treated mice. (F) Quantification of vessel density and vessel lumen area in s.c. B16F10 tumors from vehicle and FG-treated mice (n = 3). *p < 0.05; unpaired Student's *t*-test. (G) IF images of CD31-stained sections of MC38 tumors on day 16 from vehicle and FG-treated mice. (H) Quantification of vessel density and vessel lumen area in s.c. MC38 tumors from vehicle and FG-treated mice (n = 3). *p < 0.05; unpaired Student's *t*-test. Scale bar = 100 μm. Data represent the mean ± SEM. (I) IF images of CD31-stained sections of LLC tumors on day 12 from vehicle- and one-time FG-treated mice. (J) Quantification of vessel density and vessel lumen area in s.c. LLC tumors from vehicle- and FG-treated mice (n = 3). ns, not significant; unpaired Student's *t*-test.

A

Vehicle
16.3 %   80.1 %
2.2 %   1.4 %

FG
11.1 %   85.4 %
2.2 %   1.4 %

16.4 %

3.5 %

T cell gate

14.3 %

15.4 %

Mφ gate
40.0 %

Ly6C^hi Mφ   22.1 %
Ly6C^lo Mφ   44.6 %
Ly6C^neg Mφ   32.3 %

B   Veh   FG

Ly6C^hi Mφ

Ly6C^lo Mφ

Ly6C^neg Mφ

C   F4/80 / Ki-67 / DAPI

Veh

FG

D

ns

Ki-67^+ cells (% of F4/80^+ cells)

Veh   FG

E   Circulating blood

% of CD45^+ cells

CD4   CD8   Mφ   Neut   DC   Mono

Veh
FG

F   Tumor tissue

% of CD45^+ cells

CD4   CD8   Neut   DC   Mono

Veh
FG

J   Veh (LLC)   FG (LLC)

CD69 PerCP-Cy5-5-A / CD25 APC-Cy7-A

K   Veh (B16F10)   FG (B16F10)

CD69 PerCP-Cy5-5-A / CD25 APC-Cy7-A

G

CD11b^+F4/80^+ / CD45 cells (%)

Veh   FG

H

% of total Mφ

Ly6C^hi   Ly6C^low   Ly6C^neg

Veh
FG

I

% of CD45^+ cells

CD4   CD8

Veh
FG

L   LLC

CD69^+ cells (%)

CD4   CD8

Veh
FG

M   B16F10

CD69^+ cells (%)

CD4   CD8

Veh
FG

N   Lip   Clo

Veh (spleen)   FG (spleen)   Veh (spleen)   FG (spleen)
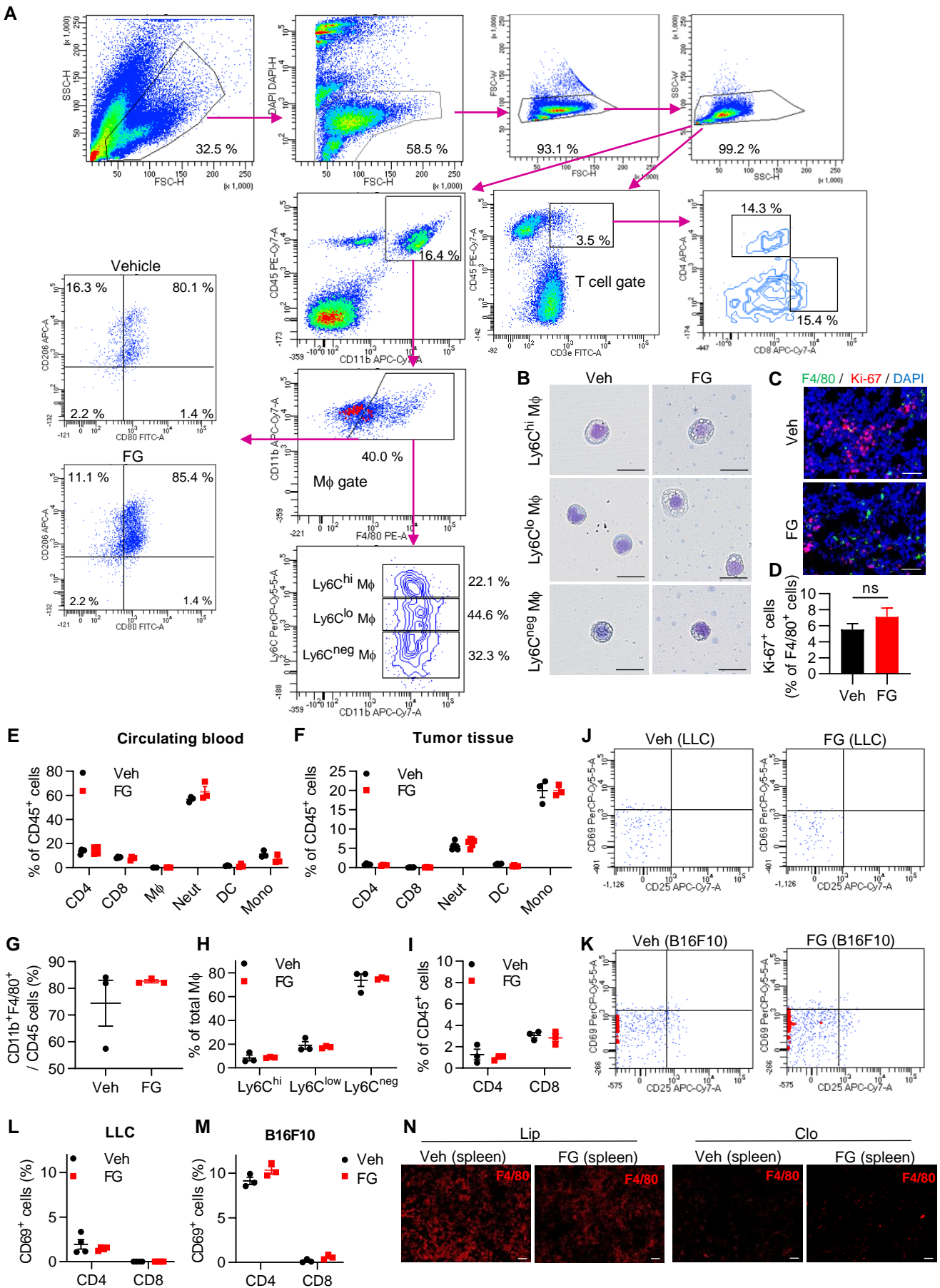
F4/80   F4/80   F4/80   F4/80

Figure S3.

Figure S3. FG inhibits tumor growth through Mφs. Related to Figure 3.

(A) Flow cytometric analysis gate strategy of Mφs and T cells in s.c. LLC tumors on day 16 (7 days after vehicle/FG treatment). (B) Morphology of $Ly6C^{hi}$, $Ly6C^{lo}$, and $Ly6C^{neg}$ Mφs. Scale bar = 20 μm. (C) IF images of Ki-67 (red)- and F4/80 (green)- stained sections of LLC tumors on day 16. Scale bar = 50 μm. (D) Quantification of the Ki-67+ cell ratio of $F4/80^+$ cells on day 16 (n = 3). ns, not significant; unpaired Student's *t*-test. (E) Quantification of the ratio of immune cells in circulating blood of LLC tumor-bearing mice on day 16 by flow cytometry (n = 3–4). (F) Quantification of the ratio of immune cells in LLC tumor tissue on day 16 by flow cytometry (n = 3–6). CD4 lymphocyte; $CD45^+CD3^+CD4^+$, CD8 lymphocyte; $CD45^+CD3^+CD8^+$, Mφ; $CD45^+CD11b^+F4/80^+$, neutrophil; $CD45^+CD11b^+Ly6G^+$, dendritic cell; $CD45^+CD11b^+CD11c^+$, monocyte; $CD45^+CD11b^+F4/80^-Ly6G^-$. (G) Quantification of the ratio of tumor-infiltrating $CD11b^+F4/80^+$ cells/$CD45^+$ cells in MC38 tumors by flow cytometry (n = 3). (H) Quantification of the $Ly6C^{hi}$, $Ly6C^{lo}$, and $Ly6C^{neg}$ Mφ ratio in MC38 tumors by flow cytometric analysis (n = 3). (I) Quantification of $CD4^+$ and $CD8^+$ lymphocyte cell ratio in MC38 tumors by flow cytometric analysis (n = 3). (J, K) Representative flow cytometric analysis of $CD45^+CD3^+$ lymphocyte cells of (J) LLC or (K) B16F10 tumor-bearing mice on day 16. (L, M) Quantification of the ratio of $CD69^+$ cells in circulating blood of (L) LLC or (M) B16F10 tumor-bearing mice on day 16 by flow cytometry (n = 3–4). (N) IF images of F4/80 (red)-stained spleen sections of LLC tumor-bearing mice treated with liposome control or clodronate liposome and vehicle or 3 mg FG. Scale bar = 50 μm.

A

VHL^fl/fl   VHL^fl/fl LysM-Cre

CD31 / DAPI

B

Vessel number / mm²

Vessel lumen area (μm²)

C

VHL^fl/fl + Veh
VHL^fl/fl + FG

Tumor volume (mm³)

Days after tumor transplantation

****

D

Tumor weight (g)

Veh   FG

VHL^fl/fl

*

E

VHL^fl/fl LysM-Cre + Veh

VHL^fl/fl LysM-Cre + FG

F

HIF1^fl/fl + Veh
HIF1^fl/fl + FG

Tumor volume (mm³)

Days after tumor transplantation

***

G

Tumor weight (g)

Veh   FG

HIF1^fl/fl

*

H

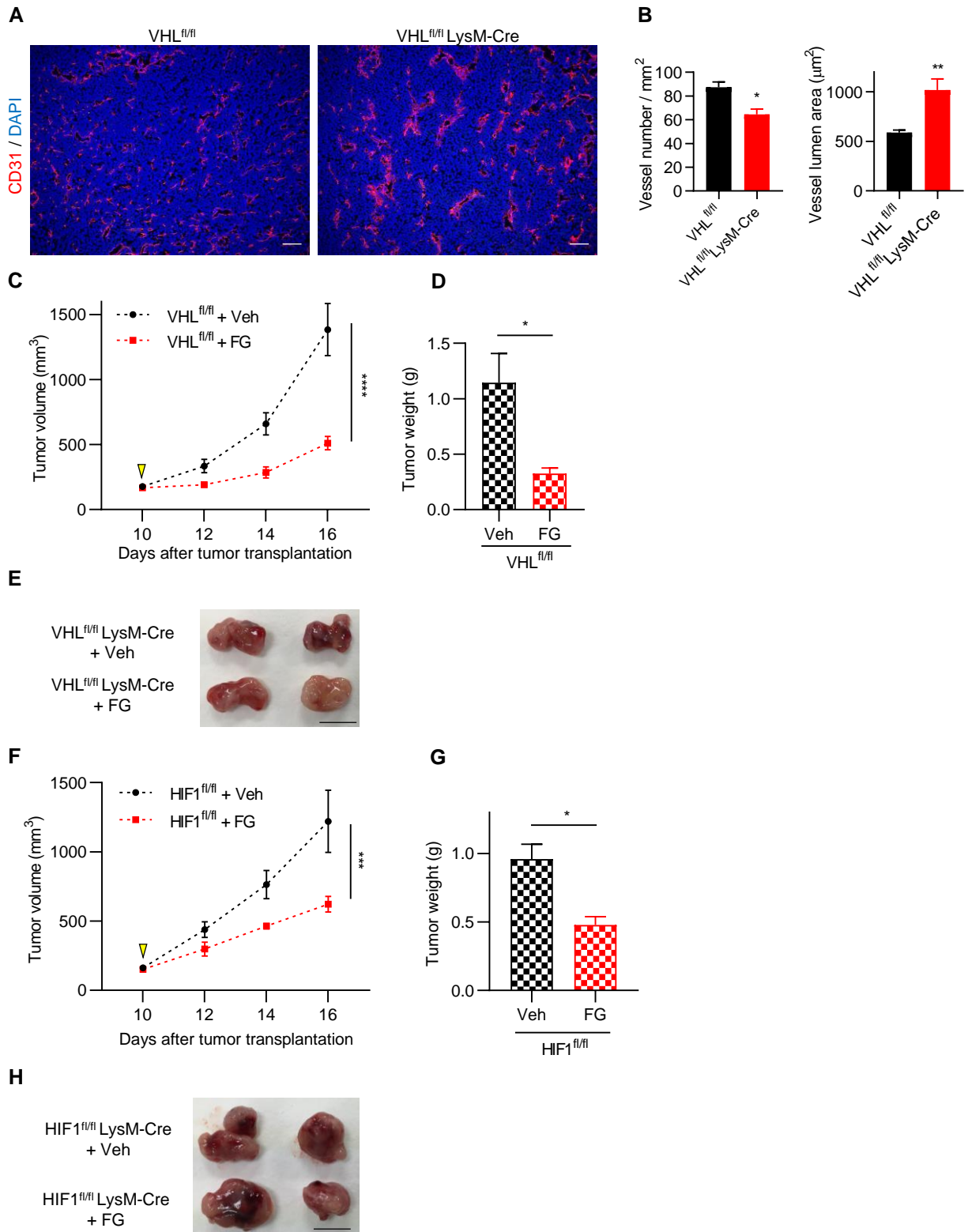HIF1^fl/fl LysM-Cre + Veh

HIF1^fl/fl LysM-Cre + FG

Figure S4.

Figure S4. FG inhibits tumor growth through Mφs via the PHD-HIF axis. Related to Figure 4.
(A) IF images of CD31 staining in VHL$^{fl/fl}$ or VHL$^{fl/fl}$ LysM-Cre mouse tumors. Scale bars = 100 μm.
(B) Quantification of vessel density and vessel luminal area in VHL$^{fl/fl}$ (n = 5) or VHL$^{fl/fl}$ LysM-Cre
mouse tumors (n = 6). *p < 0.05, **p < 0.01; Mann-Whitney test. Data represent the mean ± SEM.
(C) Tumor growth curves of the LLC tumor model of VHL$^{fl/fl}$ mice. Treatment with Veh or FG (3 mg;
treated on day 10); n = 4. ****p < 0.0001; two-way ANOVA. (D) Tumor weight on day 16 (n = 4). *p
< 0.05; Mann-Whitney test. (E) Images of tumors of VHL$^{fl/fl}$ LysM-Cre mice treated with/without FG
on day 16. Scale bar = 1 cm. (F) Tumor growth curves of the LLC tumor model of HIF1$^{fl/fl}$ mice.
Treatment with Veh (n = 4) or FG (3 mg; treated on day 10; n = 5). ***p < 0.001; two-way ANOVA.
(G) Tumor weight on day 16 (n = 4–5). *p < 0.05; Mann-Whitney test. (H) Images of tumors of
HIF1$^{fl/fl}$ LysM-Cre mice treated with/without FG on day 16. Scale bar = 1 cm.
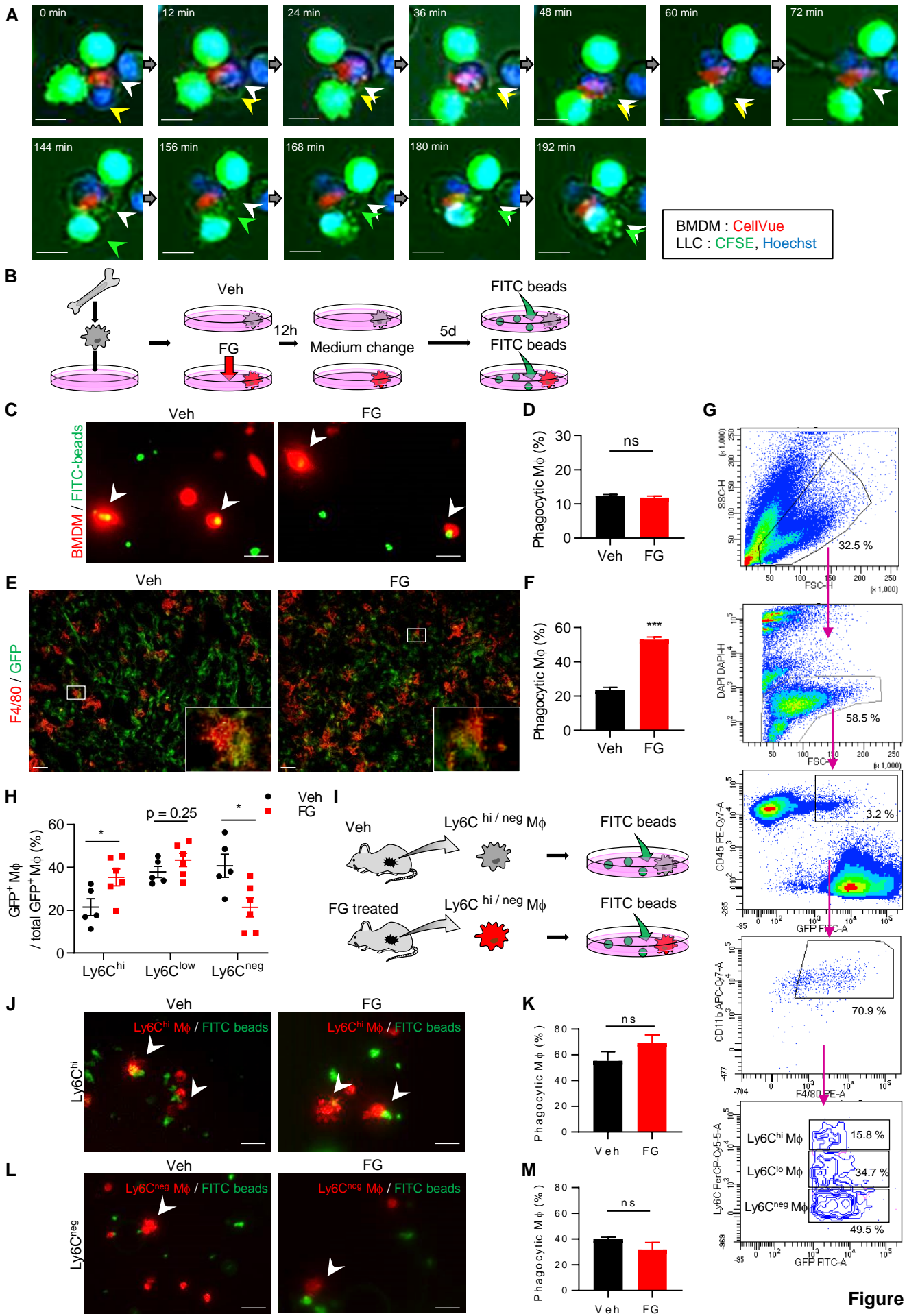
A

B

C
BMDM / FITC-beads
Veh   FG

D
Phagocytic Mφ (%)
ns
Veh   FG

E
F4/80 / GFP
Veh   FG

F
Phagocytic Mφ (%)
***
Veh   FG

G

H
GFP⁺ Mφ / total GFP⁺ Mφ (%)
● Veh
■ FG
*   p = 0.25   *
Ly6C^hi   Ly6C^low   Ly6C^neg

I
Veh   Ly6C^hi/neg Mφ   FITC beads
FG treated   Ly6C^hi/neg Mφ   FITC beads

J
Ly6C^hi
Veh   FG
Ly6C^hi Mφ / FITC beads   Ly6C^hi Mφ / FITC beads

K
Phagocytic Mφ (%)
ns
Veh   FG

L
Ly6C^neg
Veh   FG
Ly6C^neg Mφ / FITC beads   Ly6C^neg Mφ / FITC beads

M
Phagocytic Mφ (%)
ns
Veh   FG

BMDM : CellVue
LLC : CFSE   Hoechst

Figure S5.

Figure S5. FG activates phagocytosis of Ly6C-positive macrophages while TME improvement prolongs the anti-tumor effect of Mφs. Related to Figure 5.

(A) In vitro live-cell microscopy of CellVue-labeled (red) BMDM as well as CFSE (green)- and Hoechst (blue)-labeled LLC cells. BMDMs were treated with FG. Upper row, activated BMDM phagocytosed first-encountered LLC cells; lower row, activated BMDM phagocytosed second-encountered LLC cells continuously. (B) Schematic diagram of in vitro bead phagocytosis assay. (C) Images of BMDM bead phagocytosis assay. BMDM, red; FITC-beads, green. Scale bar = 20 μm. (D) Quantification of phagocytic BMDM ratio. ns, not significant; Mann-Whitney test. Two independent experiments were performed. (E) Images of IF staining of tumor phagocytic macrophages. C57BL/6 mice were transplanted with GFP-expressing LLC and treated with vehicle or 3 mg FG. Tumor sections were stained with anti-GFP (green) and anti-F4/80 (red) antibodies. Scale bar = 20 μm. (F) Quantification of phagocytic (GFP$^+$F4/80$^+$) cell number in the tumors (n = 3). ***p < 0.001; unpaired Student's t-test. (G) Flow cytometric analysis gate strategy of GFP$^+$Mφs in s.c. LLC tumors on day 16 (7 days after vehicle/FG treatment). (H) Quantification of GFP$^+$ Mφ/total GFP$^+$ Mφ ratio subdivided by Ly6C^{hi}, Ly6C^{lo}, and Ly6C^{neg} in LLC tumors by flow cytometric analysis (n = 5–6). ns, not significant (p = 0.25 vs. vehicle); *p < 0.05, **p < 0.01 vs. vehicle; Mann-Whitney test. (I) Schematic diagram of ex vivo bead phagocytosis assay. (J) Images of ex vivo phagocytosis assay. Ly6C^{hi} Mφ, red; FITC-beads, green. Scale bar = 20 μm. (K) Quantification of phagocytic Ly6C^{hi} Mφ ratio (n = 4–5). ns, not significant (p = 0.19); Mann-Whitney test. (L) Images of ex vivo phagocytosis assay. Ly6C^{neg} Mφ, red; FITC-beads, green. Scale bar = 20 μm. (M) Quantification of phagocytic Ly6C^{neg} Mφ ratio (n = 3–4). ns, not significant; Mann-Whitney test. Data represent the mean ± SEM.
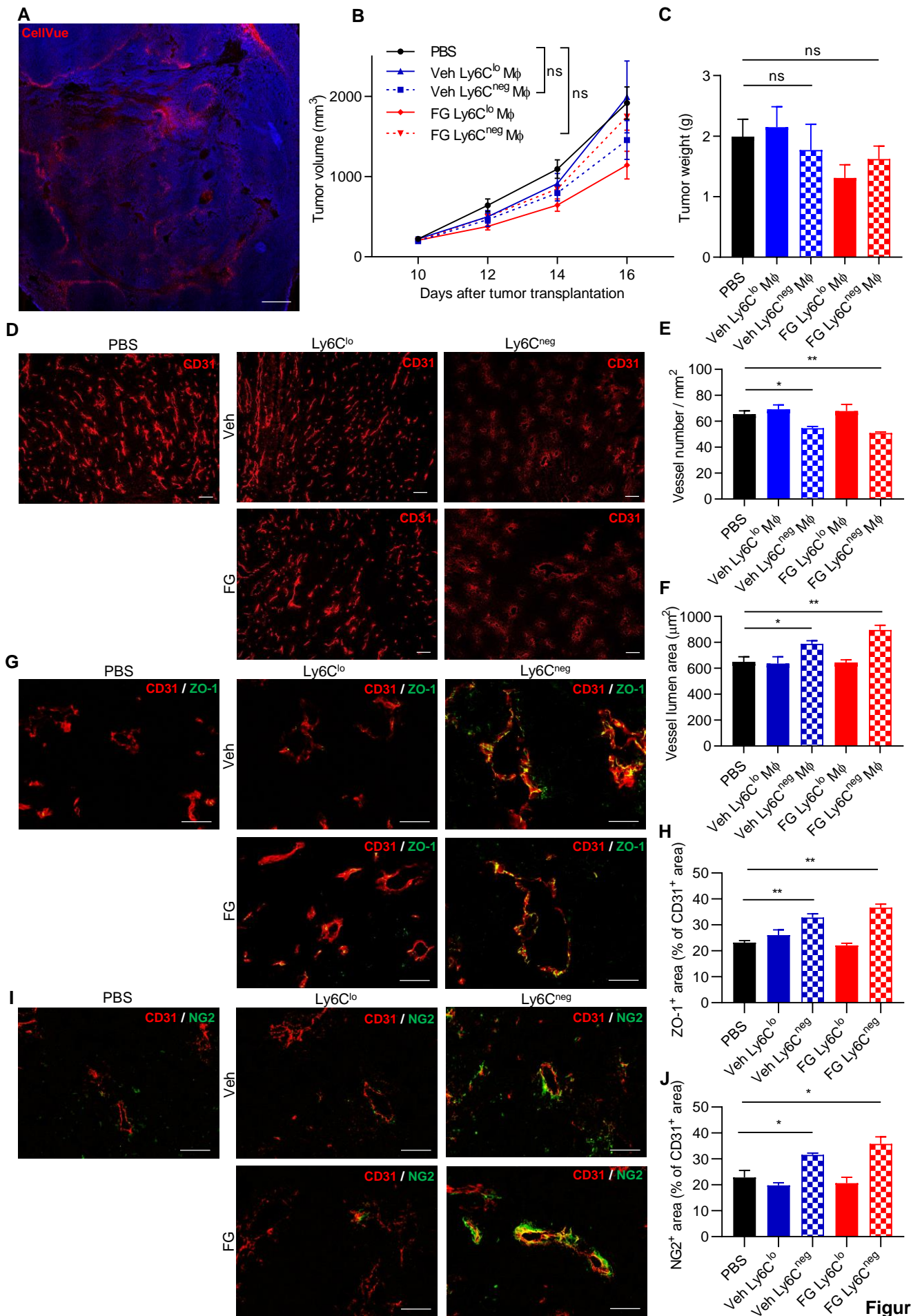
Figure S6.

Figure S6. Ly6C^neg Mφs normalize tumor vessel structure. Related to Figure 6.

(A) Histological identification of CellVue-labeled (red) transplanted Mφs. Scale bar = 1 mm. (B) Tumor growth curves of LLC tumor mouse models under conditions of PBS injection or transplantation with Ly6C^{lo} or Ly6C^{neg} Mφs sorted from vehicle/FG-treated mouse tumors (n = 5–6 per group). ns, not significant; two-way ANOVA. (C) Tumor weight was measured at the end of the experiment on day 16 (n = 5–6). ns, not significant; Mann-Whitney test. (D) IF images of CD31-stained sections of LLC tumor mouse models that were injected with PBS or received transplants of Ly6C^{lo} or Ly6C^{neg} Mφs sorted from vehicle/FG-treated mouse tumors. Scale bar = 100 μm. (E, F) Quantification of (E) vessel density and (F) vessel lumen area of s.c. LLC tumors (n = 3 per group). $p < 0.05$, $**p < 0.01$ vs. PBS; unpaired Student's t-test. (G) IF images of ZO-1 (green) and CD31 (red)-stained sections of LLC tumors. Scale bar = 50 μm. (H) Quantification of the ZO-1$^+$ area ratio in the CD31$^+$ area (n = 3). $**p < 0.01$ vs. PBS; unpaired Student's t-test. (I) IF images of NG2 (green) and CD31 (red)-stained sections of LLC tumors. Scale bar = 50 μm. (J) Quantification of the NG2$^+$ area ratio in the CD31$^+$ area (n = 3). Data represent the mean $\pm$ SEM. $*p < 0.05$, vs. PBS; unpaired Student's t-test.

Transparent Methods

Animals

All animal experiments were approved by the Institutional Animal Care and Use Committee of Osaka City University (approval number: 16022, 16021), which was approved by the Japanese Association for Accreditation for Laboratory Animal Care. Furthermore, animal research and handling were performed in strict conformance with the Institutional Animal Care and Use Committee guidelines.

C57BL/6 male mice were obtained from SLC Japan, Inc. *LysM Cre*, *VHL* floxed and *HIF1* floxed mice were obtained from Jackson Laboratories and bred in our facility. Mice were housed in cages with food and water available *ad libitum* in a 12-h light-dark cycle at 22 ± 1 °C.

Cell cultures, tumor transplant model, and PHD inhibitor treatment

LLC and B16F10 cells (RIKEN BRC) were maintained in Dulbecco's modified Eagle's medium (DMEM) and Roswell Park Memorial Institute 1640 medium (RPMI1640). These media contained 10% fetal bovine serum (FBS) and penicillin/streptomycin in 5% CO_2 and 95% room air at 37 °C. MC38 cells were maintained in DMEM containing 10% FBS, 2 mM glutamine, 0.1 mM nonessential amino acids, 1 mM sodium pyruvate, and penicillin/streptomycin in 5% CO_2 and 95% room air at 37 °C. These cells were harvested and re-suspended (at 1×10^7 cells/mL) in phosphate-buffered saline (PBS). Some of the cells (1×10^6 cells) were subcutaneously transplanted into the right flanks of 8–12-week-old mice. The mice were treated with 3 mg FG-4592 (Selleck Chemicals, Housten, TX) intraperitoneally 10 days after the tumor transplant (eligible tumor size for this study was 100–350 mm^3). Once every two days, the tumors were measured in two dimensions using a caliper. The tumor tissue volume was calculated using the formula V = (length × $width^2$)/2. The mice were sacrificed at a defined time point or when the tumor volume exceeded 4500 mm^3 or ruptured.

MTT assay

LLC cells were plated at 2×10^4 cells per well in a 96-well plate. Subsequently, FG was added to the medium at the indicated concentration (0, 50, 100, 200, and 400 μM). Cell viability was evaluated 72 h after FG treatment. Culture medium was exchanged 6 h after FG treatment. After 72 h, AlamarBlue (Bio-Rad Laboratories, Hercules, CA) reagent was added at a 1:10 volume. Following this, the plate was incubated for another 6 h at 37 °C in a 5% CO_2 incubator. Finally, optical density (OD) was measured at 570 and 600 nm, and cell viability was calculated. The experiment was performed three times with three replicates per experiment.

Establishment of stable GFP-expressing LLC

cDNAs encoding GFP1 were double digested with SalI and NotI from pAcGFP1 (Clontech, Mountain View, CA) and inserted into the SalI and NotI sites of the pEBMulti-Hyg vector (Wako Pure Chemical Industries Ltd., Osaka, Japan). This expression vector was transfected into LLC using Lipofectamine LTX Reagent (Invitrogen, Carlsbad, CA), and GFP stably expressing LLC was selected by Hygromycin B (250 μg/mL) for 7 days.

Immunofluorescence staining

Tumor tissues were sliced into frozen sections of 8-μm thickness at −20 °C and air-dried. The sectioned tissue samples were rehydrated in PBS for 10 min and fixed with 4% (w/v) cold paraformaldehyde for 10 min. The sections were then washed with PBS and permeabilized with 0.5% (v/v) Triton X-100 in PBS for 10 min, after which they were blocked in 5% normal goat serum for 30 min at room temperature (20–25 °C). The sections were incubated with the following primary antibodies, anti-CD31 (1:1000; eBioscience, San Diego, CA), anti-NG2 (1:400; Merck Millipore, Burlington, MA), anti-ZO-1 (1:400; Thermo Fisher Scientific, Waltham, MA), and anti-CC3 (1:400; Cell Signaling Technology, Danvers, MA) overnight at 4 °C. The sections were then washed with 0.1% Tween 20 in PBS and incubated for 1 h at room temperature with the appropriate fluorophore secondary antibody (AlexaFluor 488 or Cy3, goat anti-rat, or goat anti-rabbit IgG; BioLegend, San Diego CA). Finally, the sections were washed with 0.1%

Tween 20 in PBS, dehydrated with ethanol, and air-dried, after which they were mounted with

Vectashield mounting medium (Vector Laboratories, Burlingame, CA) containing 4',6-diamidino-2-

phenylindole stain (1:5000) and a cover slip.

Quantification of immunofluorescence images

Quantification of the immunofluorescent images, which were taken using a microscope (BZX-710;

Keyence, Osaka, Japan), was performed using the microscope software. At least 15 fields of images at

100, 200, or 400× magnification were analyzed for each sample. Each experiment used at least three

animals from each group.

Tumor vessel perfusion and permeability analysis

Dextran-FITC (150 kDa; Sigma-Aldrich, St. Louis, MO) was intravenously administered into the tail vein

10 min prior to sacrifice. The tumor tissues were excised and immediately frozen in liquid nitrogen. The

tumor samples were stored at −80 °C until sectioning. The tumor tissues were sectioned into 8 and 20-μm

thick sections and then observed using the BZX-710 microscope.

Detection of tumor hypoxic regions and analysis

Hypoxic regions of the tumor tissues were detected using the Hypoxyprobe™ Kit (HP3-100;

Hypoxyprobe Inc., Burlington, MA), which included pimonidazole, according to manufacturer's

instructions. In brief, pimonidazole was injected at 60 mg/kg into the tumor-bearing mice. Ninety minutes

later, the mice were sacrificed, after which the tumors were collected and cryosectioned into 4-μm thick

sections. The sections were then fixed with ice-cold acetone for 10 min, washed with PBS, and incubated

with rabbit anti-pimonidazole anti-sera (1:20) overnight at 4 °C. Subsequently, the sections were

incubated with AlexaFluor 488 conjugated goat anti-rabbit antibody (1:1000) for 1 h. Images were

acquired using the BZX-710 microscope, and the ratio of the pimonidazole-positive area was quantified

using the equipped software.

In vivo macrophage depletion

Macrophage depletion was performed according to manufacturer's instructions. In brief, mice were intraperitoneally administered 100 μL clodronate-loaded liposome (F70101C-A; FormuMax Scientific Inc., Sunnyvale, CA) or 100 μL plain control liposomes (F70101-A; FormuMax Scientific Inc.) 24 h prior to FG injection. The second administration contained 70 μL of each liposome and was administered 72 h following FG injection.

Quantitative RT-PCR (qRT-PCR)

BMDMs generated from separate mice were treated with 100 μM FG-4592 or an equal volume of DMSO for 12 h before harvesting. RNA was extracted from BMDMs with ISOGEN II (Nippon Gene, Tokyo, Japan) according to manufacturer's instructions. cDNA was reverse transcribed from 1 μg total RNA using the Prime Script RT Reagent Kit (TaKaRa Bio, Kusatsu, Japan). qPCR was then performed on the 7500 Fast Real-Time PCR system using the THUNDERBIRD SYBR qPCR Mix (Toyobo, Osaka, Japan). Five independent qRT-PCR assays were performed for each sample pair in triplicate. Relative transcript levels were normalized to 18S ribosomal RNA and analyzed using 7500 software v2.3 (Applied Biosystems, Foster City, CA).

Tumor dissociation

Perfused tumors were minced and digested with 1 mg/mL collagenase IV with 50 μg/mL DNase I for 45 min at 37 °C with shaking. Cells were filtered through a 100-μm nylon mesh and washed in isolation buffer (PBS containing 2% FBS and 2 mM EDTA). Erythrocytes were lysed using RBC lysis buffer (BioLegend). Cells were resuspended in isolation buffer, after which Fc receptors were blocked with CD16/32 blocking antibody (BioLegend) for 15 min on ice.

Flow cytometry and cell sorting

Dissociated single tumor cells were stained with the following fluorochrome-conjugated antibodies at the manufacturer's (BioLegend) recommended dilution for 30 min on ice in the dark for detecting macrophages, anti-mouse F4/80-PE (clone BM8), anti-mouse CD45 PE-Cy7 (clone 30-F11), anti-mouse Ly6C-PerCP-Cy5.5 (clone HK1.4), anti-mouse CD11b-APC-Cy7 (clone M1/70), anti-mouse CD206-APC (clone C068C2), and anti-mouse CD80 FITC (clone 16-10A1); for T cells, anti-mouse CD3ε-FITC or -PE (clone 145-2C11), anti-mouse CD45 PE-Cy7 (clone 30-F11), anti-mouse CD4-APC (clone GK1.5), and anti-mouse CD8-APC-Cy7 (clone 53-6.7) antibodies were used. To exclude dead cells, DAPI was added just before analysis. Flow cytometric analysis and cell sorting were performed on the BD LSR II or BD FACSAria III. Briefly, 100,000 cells were analyzed per sample per mouse using BD FACSDiva software ver. 8.0 (BD Biosciences). The sequential gating strategy is outlined in Supplementary Figure 3a.

Purification of CD11b-positive cells and sorting of Ly6C-positive macrophages

CD11b-positive cells were purified using the Dynabeads FlowComp Flexi Kit (Invitrogen) according to manufacturer's instructions. In brief, FcR-blocked tumor single cell suspensions were added to biotin-labelled CD11b antibody (clone M1/70; #101231; BioLegend) and incubated for 20 min at 4 °C. Cell suspensions were added to FlowComp Dynabeads, after which CD11b-positive cells were magnetically separated. FlowComp Dynabeads were released from the cells using the FlowComp Release Buffer. Bead-free cells were stained with anti-rat IgG-AlexaFluor 488 at first and subsequently stained with anti-mouse F4/80-PE, anti-mouse CD45 PE-Cy7, or anti-mouse Ly6C-PerCP-Cy5.5. To exclude dead cells, DAPI was added just before cell sorting. Cell sorting was performed using a 100-μm nozzle on a BD FACSAria III and analyzed using BD FACSDiva software.

Macrophage morphology and staining

Sorted macrophages were washed with PBS and resuspended at 5×10^4 cells/mL in PBS. Cells were attached to slides using cytospin3 and centrifuged at $200 \times g$ for 3 min. Cells were stained with the Diff-Quick Staining Kit according to manufacturer's instructions, after which the cells were observed and images captured using a microscope.

Isolation of BMDMs

Bone marrow was isolated from the tibia and femur of 8–12-week-old C57BL/6 mice and incubated in DMEM supplemented with L929 cell-conditioned medium (20%). Cells were cultured for 7 days, and the medium was replaced every 2 days. Differentiated macrophages were identified via staining for F4/80 antibody and flow cytometry.

In vitro and ex vivo beads phagocytosis assay

BMDMs and sorted macrophages were stained with CellVue Claret® (Sigma-Aldrich) according to manufacturer's instructions before seeding in a 96-well plate. Sorted cells were incubated for 2 h at 37 °C to allow them to rest after sorting. Subsequently, 24 h later, 100 μM FG or equal volume DMSO were added to the culture media. After 12 h, Latex Beads-Rabbit IgG-FITC Complex (Cayman Chemical, Ann Arbor, MI) was added to the culture media (1:400). After 45 min, phagocytic macrophages were imaged, counted using the BZX-710 microscope, and analyzed with the equipped software. Over 800 cells were analyzed per group.

Coculture phagocytosis assay

BMDMs were stained with CellVue Claret® (Sigma-Aldrich) according to manufacturer's instructions before seeding 5×10^4 cells/well in a 24-well plate. After 24 h, 100 μM FG or equal volume DMSO were added to the culture media. After 12 h, 5×10^4 LLC were seeded in each well. Before seeding, 1 μg/mL Hoechst 33342 was added to the LLC culture media and incubated for 1 h, after which the LLC cells were trypsinized and stained with CFSE according to manufacturer's instructions. After LLC seeding, images

were immediately acquired using the IN Cell Analyzer 2500HS (GE Healthcare, Chicago, IL) or the BZX-710 microscope.

Transplantation of sorted macrophages into tumor tissues

Sorted macrophages were spun down in PBS and resuspended in 20 µL PBS. For FG treatment, sorted macrophages were seeded in 10-cm dishes and incubated with/without 100 µM FG for 12 h. Subsequently, macrophages were harvested and resuspended in 20 µL PBS. The mice were anaesthetized on day 10 after tumor transplantation, after which 1×10^5 cells were injected into the tumor using a 26-gauge needle. After intra-tumor injection of the macrophages, the tumors were measured once every 2 days. The mice were then sacrificed on day 16.

Statistical analysis

Statistical analyses were performed using the unpaired t-test followed by a Bonferroni's post-hoc test via GraphPad Prism software (ver 7.02; GraphPad Software Inc., La Jolla, CA). P values < 0.05 were considered statistically significant. All analysis was performed using a two-tailed analysis.